

SDSS-IV MaNGA: Internal mass distributions and orbital structures of early-type galaxies and their dependence on environment

Yunpeng Jin^{1,2*}, Ling Zhu³, R. J. Long^{4,1,5}, Shude Mao^{4,1}, Lan Wang¹, Glenn van de Ven^{6,7}

¹National Astronomical Observatories, Chinese Academy of Sciences, 20A Datun Road, Chaoyang District, Beijing 100101, China

²University of Chinese Academy of Sciences, Beijing 100049, China

³Shanghai Astronomical Observatory, Chinese Academy of Sciences, 80 Nandan Road, Shanghai 200030, China

⁴Department of Astronomy and Tsinghua Centre for Astrophysics, Tsinghua University, Beijing 100084, China

⁵Jodrell Bank Centre for Astrophysics, Department of Physics and Astronomy, The University of Manchester, Oxford Road, Manchester M13 9PL, UK

⁶Department of Astrophysics, University of Vienna, Türkenschanzstrasse 17, 1180 Vienna, Austria

⁷European Southern Observatory, Karl-Schwarzschild-Str. 2, 85748 Garching b. München, Germany

Accepted XXX. Received YYY; in original form ZZZ

ABSTRACT

In our earlier 2019 paper, we evaluated the reliability of Schwarzschild’s orbit-superposition dynamical modelling method in estimating the internal mass distribution, intrinsic stellar shapes and orbit distributions of early-type galaxies (ETGs) taken from the Illustris cosmological simulation. We now apply the same techniques to galaxies taken from the integral-field survey Mapping Nearby Galaxies with APO (MaNGA), using a sample of 149 ETGs in the mass range of $10^{9.90} \sim 10^{11.80} M_{\odot}$ and made up of 105 central and 44 satellite galaxies. We find that low-mass ETGs with $\log(M_*/M_{\odot}) < 11.1$ have an average dark matter fraction of ~ 0.2 within one effective radius R_e , tend to be oblate-like, and are dominated by rotation about their minor axis. High-mass ETGs with $\log(M_*/M_{\odot}) > 11.1$ have an average dark matter fraction of ~ 0.4 within one effective radius R_e , tend to be prolate-like, and are dominated by rotation about their major axis and by centrophilic orbits. The changes of internal structures within one R_e are dominated by the total stellar mass of the individual galaxies. We find no differences of internal structures between central and satellite ETGs for the same stellar masses. However, for similar stellar mass and colour distributions, we find that ETGs more prolate-like, or with more hot orbits, tend to have higher close neighbour counts at $r_p \sim 40$ kpc.

Key words: galaxies: elliptical and lenticular, cD – galaxies: kinematics and dynamics – galaxies: structure – galaxies: fundamental parameters

1 INTRODUCTION

In the currently accepted paradigm of cosmological structure formation, it is widely believed that galaxies form and evolve in cold dark matter haloes. In the Λ CDM framework, galaxies undergo hierarchical evolution, with smaller galaxies merging to form larger galaxies. The merger history of a galaxy is thought to be one of the major factors that determines the internal kinematic structures of galaxies (e.g., White 1979; Fall & Efstathiou 1980; Park et al. 2019). However, galactic structures can also evolve via secular processes, perhaps due to disk internal instabilities, or heating from bars or spiral arms (see, for example, Minchev & Quillen 2006; Saha et al. 2010).

Statistical studies show that structural properties of galaxies

vary as a function of galaxy stellar mass (e.g., bulge-to-total mass fraction, Weinzierl et al. 2009; size and Sérsic index, Wuyts et al. 2011; Hubble type, Bernardi et al. 2010 and Calvi et al. 2012; velocity dispersion σ_e and size, Cappellari et al. 2013b). The environment of a galaxy also plays an important role in creating structures via actions such as tidal stripping or ram pressure. For example, a bar could be induced by tidal forces in a cluster environment (Lokas et al. 2016). There are a number of ways of quantifying the effect of environment on galaxies. Galaxy groups have been separated into central and satellite galaxies (e.g., Zheng et al. 2005; Berlind et al. 2006; Yang et al. 2007, 2008) based on the halo occupation distribution. Unsurprisingly, central and satellite galaxies have both similarities and differences. Satellites are older and metal richer than centrals of the same stellar mass (Pasquali et al. 2010), while they both follow a qualitatively similar gas-phase metallicity (Pasquali et al. 2012). Late-type satellites are found to be redder,

* E-mail: jyp199333@163.com

smaller and more concentrated than late-type centrals for a given stellar mass (Weinmann et al. 2009). Such differences do not exist between early-type centrals and satellites (Huertas-Company et al. 2013). There is no significant difference of bulge-to-total mass ratio B/T between centrals and satellites (Bluck et al. 2019). Quite apart from this separation into centrals and satellites, a galaxy’s local density environment can affect its properties, such as morphology (Postman & Geller 1984; Dressler et al. 1997; Goto et al. 2003; Tanaka et al. 2004), or luminosity and colour (Hogg et al. 2003; Blanton et al. 2005a; Deng et al. 2009). A galaxy’s local density environment can be quantified by the number of neighbours $N_{\text{neighbour}}$ within a certain projected radius r_p (Li et al. 2008). The number of neighbours seems to be related to a galaxy’s internal structures, with, for example, pseudo-bulge and pure-disc galaxies showing a strong excess in close neighbour counts when compared to control galaxies with similar stellar masses (Wang et al. 2019).

In recent years, Integral Field Unit (IFU) surveys such as SAURON (Bacon et al. 2001), ATLAS^{3D} (Cappellari et al. 2011), CALIFA (Sánchez et al. 2012), SAMI (Bryant et al. 2015), MaNGA (Bundy et al. 2015; Blanton et al. 2017) and MUSE (Bacon et al. 2017) provide us with much data about galaxies potentially allowing their structure, formation and evolution to be investigated. The MaNGA survey (Mapping Nearby Galaxies at Apache Point Observatory), one of three core programmes in SDSS-IV (the fourth-generation Sloan Digital Sky Survey), aims to observe a sample of 10,000 nearby galaxies, and is the survey from which we take our galaxy data.

Using data from IFU surveys, we are able to investigate the internal kinematics of galaxies. Greene et al. (2018) analyzed the two-dimensional stellar kinematic maps of MaNGA galaxies, and found that there is no residual differences in angular momentum content λ_R (Emsellem et al. 2011) between central and satellite early-type galaxies when carefully matching the stellar mass distributions. However, λ_R is directly calculated from kinematic maps on the observational plane and can only incorporate line-of-sight kinematics. Our earlier paper Jin et al. (2019), as a precursor to this paper, evaluated the capabilities of Schwarzschild orbit-superposition technique (Schwarzschild 1979) using data from the Illustris cosmological simulation (Vogelsberger et al. 2014a,b; Genel et al. 2014; Nelson et al. 2015), and we continue with Schwarzschild’s method and the same implementation here. Stellar dynamical modelling tools such as Schwarzschild’s method are only able to provide partial insight into the three-dimensional internal kinematic structures underlying the line-of-sight kinematics. Given the limitations of the instrumentation currently available for observing external galaxies and for reasons of deprojection non-uniqueness, these tools can not identify the true three-dimensional structures of a galaxy but can at least give an indication as to what they might be like.

Early-type galaxies (ETGs) show complicated structures in their kinematic maps, but can be split on their kinematics into two classes, fast rotators and slow rotators. According to Cappellari (2016), this split into two classes also indicates two major channels of galaxy formation. Fast-rotator ETGs start as star forming disks and evolve through a set of processes dominated by gas accretion, bulge growth and quenching. By comparison, slow-rotator ETGs assemble near the centre of massive haloes via intense star formation at high redshift, and evolve from a set of processes dominated by gas poor mergers. Environment is believed to play an important role in the quenching of star formation (Peng et al. 2010). However, the extent to which environmental processes could also affect internal galaxy structures is unclear.

For the research documented here, we have focussed on ETGs only, and our intention is to examine the relationships between internal structures, evolution and environments. To this end, our specific objectives, using a sample of central and satellite ETGs taken from MaNGA, are

- (i) to model the galaxies individually using Schwarzschild’s method and determine their mass distributions, intrinsic stellar shapes and internal orbit distributions,
- (ii) to examine statistically the differences and similarities between central and satellite ETGs, and
- (iii) to assess the role of the environment in the galaxies’ evolution.

Our sample of 149 galaxies is to date the largest sample of ETGs modelled using Schwarzschild’s method. Zhu et al. (2018b) used the same triaxial Schwarzschild implementation (van den Bosch et al. 2008) in their modelling of 300 CALIFA galaxies but over 70 percent of their galaxy sample were LTGs. We use cosmological parameters from Planck Collaboration et al. (2014): $H_0 = 67.8 \text{ km} \cdot \text{s}^{-1} \cdot \text{Mpc}^{-1}$, $\Omega_\Lambda = 0.692$ and $\Omega_m = 0.308$.

The structure of the paper is as follows. In § 2, we describe at a high level the approach we take which is based strongly on our experiences of having evaluated Schwarzschild’s method with simulation data (Jin et al. 2019). In § 3, our galaxy sample selection criteria and the MaNGA data we use are presented. Low level technical details about our modelling are given in § 4. In § 5, we analyze the model results for an example galaxy. The statistical results from modelling our galaxy sample are shown in § 6, with the local environment impact being considered in § 7. We discuss our findings in § 8, and conclude our investigation in § 9.

2 APPROACH

As indicated in § 1, we are modelling our individual galaxies using Schwarzschild’s method, and we use the implementation produced by van den Bosch et al. (2008) which allows us to model triaxial stellar components. A systematic evaluation of this implementation, using data from the Illustris simulation, has already been presented in our companion paper (Jin et al. 2019). In the evaluation, nine early-type simulated galaxies with a range of triaxiality were selected and used to create mock IFU data with similar data quality to that of MaNGA. Five line-of-sight projections of each galaxy were made giving a total of 45 galaxies to be modelled. We assessed estimates of the mass profiles including both stellar and dark matter components, galaxy intrinsic stellar shapes, and orbit circularities. The masses and shapes were reasonably close to the true values of the simulated galaxies while the 3D orbit circularities were plausible. The quantified model biases and uncertainties are used in this investigation (see § 6.1 for details).

In this paper, we set up our Schwarzschild models for our MaNGA galaxies in the same way as described in Jin et al. (2019). We refer the readers to van den Bosch et al. (2008) and Jin et al. (2019) for fuller details on triaxial Schwarzschild modelling. The galaxy gravitational potentials in our modelling are generated in three parts, as in Jin et al. (2019): a triaxial stellar component, whose mass is calculated using the Multi-Gaussian Expansion (MGE) formalism (Emsellem et al. 1994; Cappellari 2002); a dark matter halo, which is assumed to follow the spherical Navarro-Frenk-White (NFW) profile (Navarro et al. 1996); and a central super massive black hole which is treated as a point source. There are six free parameters describing the overall potential which must be

determined. As in our earlier paper, we run a grid based parameter search to determine the best-fitting parameters for each galaxy. The search itself requires 1000 to 2000 separate Schwarzschild models per galaxy to be run.

Previous research using the [van den Bosch et al. \(2008\)](#) implementation indicates that it has been well-utilised over a 10 year period prior to our work. Using mock galaxies based on theoretical Abel models ([Dejonghe & Laurent 1991](#); [Mathieu & Dejonghe 1999](#)), [van de Ven et al. \(2008\)](#) estimated internal orbital structures and [van den Bosch et al. \(2009\)](#) investigated how well the model could match the true intrinsic stellar shapes. [van den Bosch & de Zeeuw \(2010\)](#) modelled two individual galaxies NGC 3379 and M32 and obtained their black hole masses. [Zhu et al. \(2018a\)](#) investigated the orbits of CALIFA spiral galaxies, and [Zhu et al. \(2018b\)](#) evaluated how well the model described the true circularity distributions of over 100 mock galaxies from different simulations, and also studied the statistical circularity distributions for 300 CALIFA galaxies.

Having obtained our best-fitting Schwarzschild models, we need a stellar mass for each galaxy that can be used to compare our results with other results from the literature. Unfortunately, many of these literature results are framed not using dynamical stellar masses but masses obtained from population synthesis techniques. In addition results from investigating orbits and orbit structures are quoted using stellar masses only and not the total mass including dark matter. In this paper, we choose to discard the dynamical stellar masses resulting from using Schwarzschild method and substitute instead stellar masses determined by stellar population synthesis. This approach is not completely satisfactory and we will return to it in the discussion in § 8.

In assessing the role of environment in the evolution of our galaxies, we do so by considering how many other galaxies are in the vicinity of each galaxy. We utilise galaxy neighbour counts ([Li et al. 2008](#)), and study whether or not there is any variation in the internal properties of our galaxies with differing neighbour counts.

3 DATA

3.1 MaNGA

The galaxy selection criteria of MaNGA depend on i-band absolute magnitude and ensure that all galaxies have similar angular size so that the IFUs can cover 1.5 to 2.5 effective radii per galaxy ([Wake et al. 2017](#)). MaNGA uses the 2.5m Sloan Telescope ([Gunn et al. 2006](#)) and employs 17 hexagonal fibre bundles that vary in diameter from 12'' (19 fibres) to 32'' (127 fibres) ([Drory et al. 2015](#)). The twin multi-object fibre spectrographs cover a wide range of wavelengths, from 360 Å to 1030 Å ([Smee et al. 2013](#)). Other important information about MaNGA includes the observing strategy in [Law et al. \(2015\)](#), the survey design in [Yan et al. \(2016a\)](#), the spectrophotometry calibration technique in [Yan et al. \(2016b\)](#), and the data reduction pipeline (DRP) in [Law et al. \(2016\)](#).

3.2 Sample Selection

We select central galaxies and satellites by matching the galaxy catalogue from MaNGA MPL4 (MPL = MaNGA Product Launches; MPL4 contains a total of 1390 galaxies) and the galaxy group catalogue ([Yang et al. 2007](#)) of SDSS DR7 (Data Release). The bright-

est galaxy in a group is tagged as the central galaxy and all others as satellite galaxies ([Yang et al. 2008](#)). In addition, if the brightest galaxy is not the most massive one in a group, we remove all the galaxies in this group to avoid any possible effects caused by confusing centrals and satellites. In total we have 907 central and 357 satellite galaxies. As the data quality of low luminous galaxies is not good enough for our modelling, we manually choose galaxies with SDSS r-band model magnitude brighter than 15, and arrive at 290 central galaxies and 122 satellites. Using the ETG classification from Galaxy Zoo 1 ([Lintott et al. 2011](#)), 141 central and 58 satellite ETGs are then selected. From a visual inspection of these ETGs based on both SDSS images and kinematic maps in MaNGA MPL5 data-analysis pipeline (DAP, [Westfall et al. 2019](#)), we reduce our candidate galaxies further still. The main criteria are as follows. Firstly, we exclude galaxies that are merging, or have ring structures, dust lanes, foreground stars or anything else that will affect data quality or is hard to model. Secondly, where we have multiple observations of the same galaxy, we choose the observations with the most measurement points. Finally we arrive at 105 central and 44 satellite ETGs and we take these as our sample.

We take the Petrosian half-light radii in the NASA-Sloan Atlas catalog ([Blanton & Moustakas 2009](#)) as the effective radii R_e of our galaxies. We show the distribution of our sample on a population synthesis total stellar mass M_* (see § 4.3 for details) versus effective radius R_e plot in Fig. 1, where we also compare our sample with the complete MaNGA ETG sample in MPL6. The two samples are slightly different on the marginalized mass and size distribution in the mass range of $10.3 < \log(M_*/M_\odot) < 11.8$, but follow the same mass-size trend, which means our sample from the early MPL4 catalogue is representative of the later, larger MPL6 ETG sample. The stellar masses of the central ETGs range from $10^{10.15}$ to $10^{11.80} M_\odot$, while satellites range from $10^{9.90}$ to $10^{11.44} M_\odot$.

3.3 Individual galaxy data

As mentioned in [Jin et al. \(2019\)](#), the Schwarzschild implementation uses both luminosity and kinematics as model constraints, including the line of sight mean velocity V and velocity dispersion σ . For the luminosity constraints, we apply the MGE method ([Cappellari 2002](#)) to model the SDSS r-band image mosaics. The MGE fitted two-dimensional surface brightness together with the deprojected three-dimensional luminosity density are used as our model luminosity constraints. For the kinematic constraints, we use data from MaNGA MPL5 (internal release of SDSS DR14, [Abolfathi et al. 2018](#)) which was generated by the MaNGA data-analysis pipeline (DAP, [Westfall et al. 2019](#)). We show our model constraints for an example MaNGA galaxy, 8247-6101 (plate-IFU), in Fig. 2 for the surface brightness and contours from the MGE fitting process, and in Fig. 3 for the point-symmetrised mean velocity V and velocity dispersion σ .

4 MODELLING

As indicated earlier, we are using two modelling regimes, Schwarzschild modelling and stellar population synthesis. The Schwarzschild modelling method that we use in this work is fully described in [Jin et al. \(2019\)](#). Here, we describe how the values of free parameters and confidence levels are found using Schwarzschild's method. The grid search of free parameters and information about the best-fitting model are set out in § 4.1. The

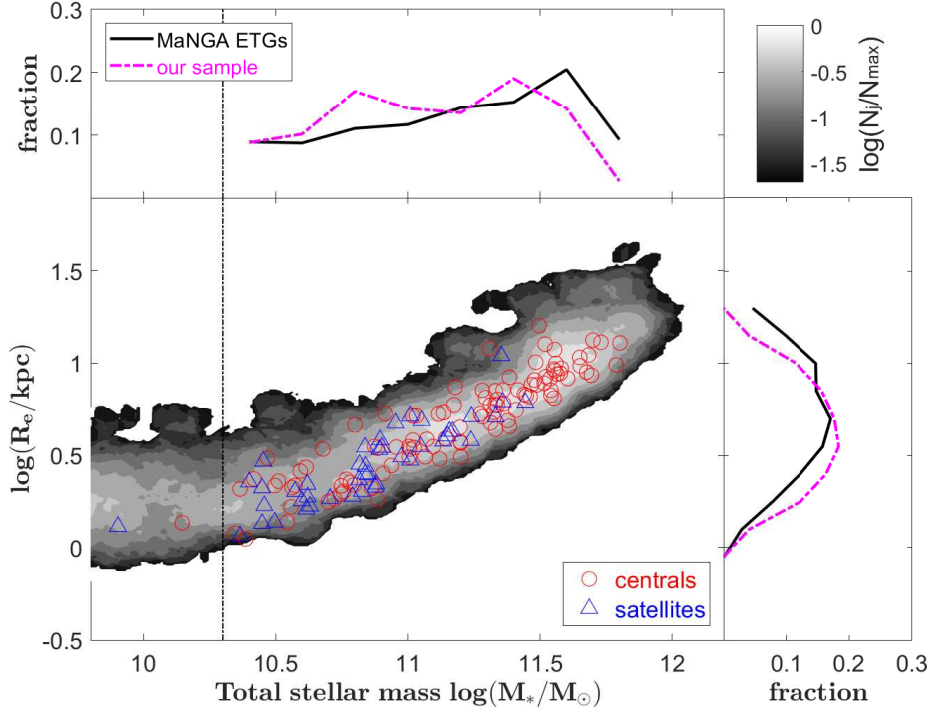


Figure 1. The distribution of our sample on a total stellar mass M_* versus effective radii R_e plot. The red circles represent central ETGs and the blue triangles are for satellite ETGs. The vertical black dashed line indicates the stellar mass $\log(M_*/M_\odot) = 10.3$. The background colour map shows the number count distribution of all ETGs in the MaNGA MPL6 with stellar mass $\log(M_*/M_\odot) > 9.7$, with their number densities $\log(N_j/N_{\max})$ being indicated by the colour bar. N_j is the number of galaxies in mass vs effective radius bin j , and N_{\max} is the maximum of the N_j . We calculate the marginalised fractions of galaxies with $\log(M_*/M_\odot) > 10.3$ by mass and size, and show them in the figure. The black solid lines are for overall ETGs while the magenta dashed lines are for our sample. The two samples are slightly different on the marginalized mass and size distribution in the mass range of $10.3 < \log(M_*/M_\odot) < 11.8$, but follow the same mass-size relation.

confidence levels we describe in § 4.2 are used for estimating statistical errors in our model parameters.

We use stellar population synthesis to calculate the galaxy stellar masses we use for comparison purposes. In § 4.3, we present how we calculate these stellar masses.

4.1 Parameter grids and the best-fitting model

We have a total of six free parameters in our models. Three are intrinsic stellar shape parameters: the medium to long axis ratio $p = b/a$, the short to long axis ratio $q = c/a$, and the major axis compression factor $u = a_{2D}/a_{3D}$ between the two-dimensional and three-dimensional Gaussians in the MGE procedure. Two are NFW dark matter halo parameters: the dark matter concentration c_{NFW} and the virial mass in units of the total stellar mass $f_{\text{NFW}} = M_{200}/M_*$. Lastly, we have the stellar mass to light ratio M_*/L . Section 4 in Jin et al. (2019) contains full descriptions of these parameters.

We find the best-fitting model by grid searching across the parameter space. The best-fitting model is defined as the model with minimum kinematic χ^2 :

$$\chi^2 = \sum_{n=1}^{N_{\text{kin}}} \left[\left(\frac{V_{\text{model}}^n - V_{\text{obs}}^n}{V_{\text{obserr}}^n} \right)^2 + \left(\frac{\sigma_{\text{model}}^n - \sigma_{\text{obs}}^n}{\sigma_{\text{obserr}}^n} \right)^2 \right], \quad (1)$$

where V_{model}^n , σ_{model}^n are the model predictions for the n -th bin and V_{obs}^n , σ_{obs}^n are the observed values, while V_{obserr}^n , σ_{obserr}^n represent

the observational errors. N_{kin} is the number of bins in the kinematic maps. We assume several groups of initial parameters as starting points for the Schwarzschild models. After these first models have been run, we adopt an iterative process for exploring the parameter space. We create new models around the existing models with lower kinematic χ^2 values by changing the values of parameters in fixed step sizes. This iteration is repeated until we obtain a χ^2 minimum region. We then reduce the step sizes by half to create more models around this region, and continue the iteration. By restricting the minimum step sizes for the free parameters, we eventually find the best-fitting model from a minimum in the kinematic χ^2 , and surrounded by enough models for the evaluation of statistical errors. The parameter space for a complete model run for galaxy 8247-6101 is shown in Fig. 4. The dots represent the parameters we have explored. The largest red dot with an asterisk inside indicates the best-fitting model, and whose kinematic map is presented in Fig. 5. Other coloured and small black dots indicate respectively the models within and outside the 2σ confidence level (see § 4.2 for the definition of the confidence level). Note that the axis ratios $p = b/a$ and $q = c/a$ here correspond to the three-dimensional de-projection of the flattest Gaussian, and not the average axis ratios of this galaxy.

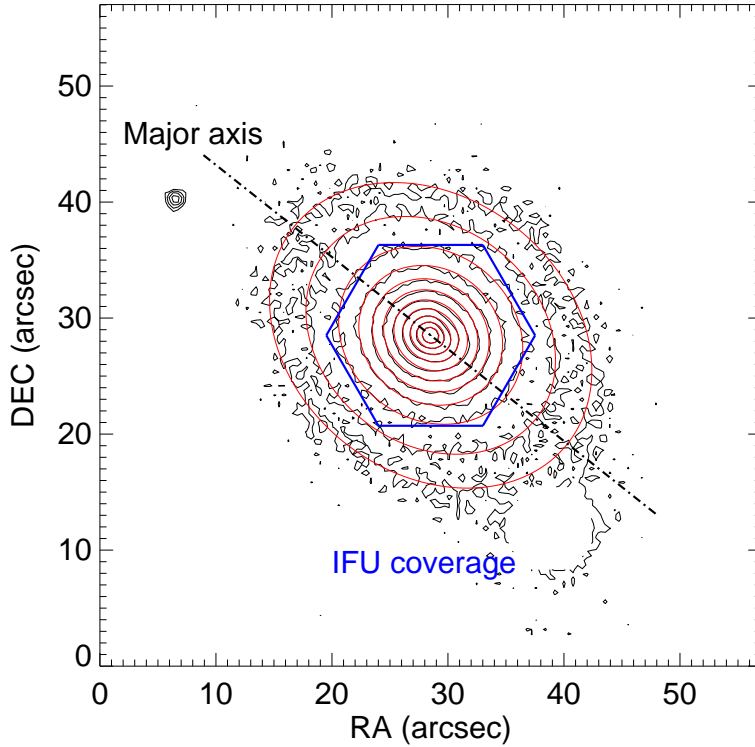


Figure 2. Surface brightness contours and MGE fitting results for example MaNGA galaxy 8247-6101 (plate-IFU). The blue hexagon shows the coverage of the IFU fibres. The black contours represent the original image while the red contours are from the MGE model. The contour interval is equal to 0.5 magnitude. The black dashed line indicates the photometric major axis.

4.2 Confidence levels

In the Schwarzschild method, using the standard definition of $\Delta\chi^2$ as a confidence level is not feasible, because the models are non-linear in the model parameters, and, from a practical perspective, model fluctuations dominate the variation in χ^2 . We choose to follow our earlier paper [Jin et al. \(2019\)](#), which is based on [van den Bosch et al. \(2008\)](#), but with an added re-scale factor of 2 before the square root term, and define the 1σ confidence level as

$$\Delta\chi^2 \equiv \chi^2 - \chi_{\min}^2 < 2 \times \sqrt{2(N_{\text{obs}} - N_{\text{par}})} \equiv \Delta\chi_{\text{CL}}^2, \quad (2)$$

where χ_{\min}^2 means the chi-square of the best-fitting model. N_{obs} is the number of kinematic constraints ($N_{\text{obs}} = 2N_{\text{kin}}$ as we use V and σ as model constraints). N_{par} is the number of free parameters ($N_{\text{par}} = 6$ here). The models whose χ^2 satisfy this inequality are included for calculating the statistical uncertainties of the model parameters for single data analysis. The maximum and minimum values of the parameters or properties in these models are treated as upper and lower limits in 1σ error regions.

4.3 Stellar masses

Utilising the algorithm described in [Li et al. \(2017\)](#), the stellar masses within R_e of all the MaNGA galaxies are obtained through stellar population synthesis (SPS) techniques, using the pPXF full spectrum fitting software ([Cappellari & Emsellem 2004; Cappellari 2017](#)), the MILES stellar libraries ([Vazdekis et al. 2010](#)), and by assuming a Chabrier initial mass function (IMF, [Chabrier 2003](#)). The total stellar mass M_* of a galaxy is estimated as twice the stellar mass within R_e . The scatter of stellar masses calculated in this way, by assuming a particular IMF, is typically less than 0.1 dex

([Li et al. 2017; Ge et al. 2018](#)). Assuming a Salpeter IMF ([Salpeter 1955](#)) leads to a systematical shift of 0.25 dex in stellar mass.

As overviewed in § 2, we are able to obtain the dynamical stellar mass constrained by our Schwarzschild modelling for the galaxies in our sample. For convenient comparison with the whole MaNGA sample and previous results in the literature, we use stellar masses M_* estimated by SPS throughout the paper unless stated otherwise. For our sample, in Fig. B1, we show a comparison of stellar masses obtained from these two methods for our sample. Using one instead of the other will not significantly change our results. However, this approach of mixing data from different modelling regimes is not satisfactory and we discuss the matter further in § 8.

5 RESULTS FOR AN INDIVIDUAL GALAXY

In this section, we show the detailed results for one galaxy. It is not practical to show the detailed results for all 149 galaxies in our sample. Given our objectives in § 1, we focus on the following galaxy properties: the mass distribution including both stellar and dark matter components, the intrinsic stellar shape, and the internal orbit circularity distribution. In this section, we continue to take galaxy 8247-6101 as an example and show its detailed model results.

Fig. 6 shows the mass profiles from the best-fitting model for our example galaxy (the black hole mass is negligible). The black, red and blue lines indicate the profiles of the total mass $M_{\text{tot}}(< r)$, stellar mass $M_*(< r)$ and dark matter $M_{\text{dark}}(< r)$, respectively. The error bars represent the 1σ confidence level defined as in § 4.2. The effective radius R_e of this galaxy is 5.35 arcsec (2.79 kpc) and

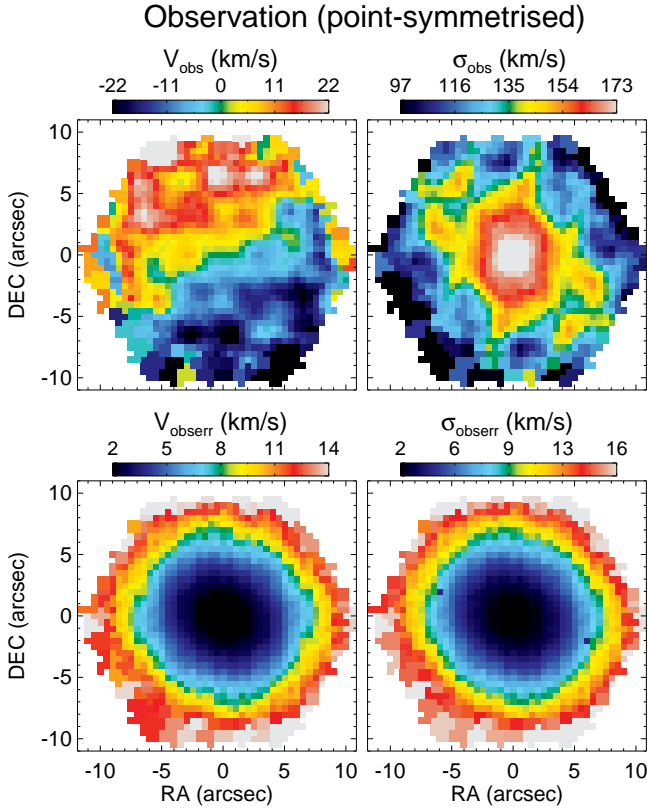


Figure 3. The point-symmetrised observational kinematic data for galaxy 8247-6101. The first row shows the line of sight mean velocity V_{obs} and velocity dispersion σ_{obs} , while the second row shows the corresponding observational errors, V_{obserr} and σ_{obserr} .

the maximum IFU coverage R_{max} (the blue hexagon in Fig. 2) is 9 arcsec.

We present the variation of intrinsic stellar shape as a function of radius r for the best-fitting model in Fig. 7. The red line represents the medium to long axis ratio $p(r) = b/a$ and the blue line indicates the short to long axis ratio $q(r) = c/a$. The triaxial parameter $T(r) = (1 - p(r)^2)/(1 - q(r)^2)$ (Binney & Tremaine 2008), which indicates galaxy triaxiality, is shown by the black line. The error bars have the same meaning as Fig. 6.

The orbit circularity parameters λ_z and λ_x , which represent the rotations about the minor axis (z -axis) and the major axis (x -axis), are defined as a ratio of time-averaged quantities (Zhu et al. 2018a,b; Jin et al. 2019)

$$\begin{cases} \lambda_z = \overline{L_z} / (\overline{r} \times \overline{V_{\text{rms}}}), \\ \lambda_x = \overline{L_x} / (\overline{r} \times \overline{V_{\text{rms}}}), \end{cases} \quad (3)$$

where $\overline{L_z} = \overline{xv_y - yv_x}$, $\overline{L_x} = \overline{yv_z - zv_y}$, $\overline{r} = \sqrt{x^2 + y^2 + z^2}$ and $\overline{V_{\text{rms}}} = \sqrt{v_x^2 + v_y^2 + v_z^2 + 2v_xv_y + 2v_xv_z + 2v_yv_z}$. Typical short-axis tube orbits have $0 < \lambda_z < 1$ and $\lambda_x \sim 0$, while for long-axis tube orbits we have $\lambda_z \sim 0$ and $0 < \lambda_x < 1$. Box orbits that dominate by centrophilic orbits satisfy both $\lambda_z \sim 0$ and $\lambda_x \sim 0$. Negative values of orbit circularity mean the orbits are counter-rotating. We calculate the circularity parameters for each orbit. Based on the orbit weights from the best-fitting model, we obtain the probability density distribution of the orbits with $\overline{r} < R_e$ on the $\lambda_z - \lambda_x$ plane shown in Fig. 8. Following Jin et al. (2019), we first divide orbits with differ-

ent λ_z into cold ($\lambda_z \geq 0.8$), warm ($0.25 < \lambda_z < 0.8$), hot ($-0.25 \leq \lambda_z \leq 0.25$) and counter-rotating orbits ($\lambda_z < -0.25$). In order to distinguish long-axis tube orbits and box orbits from hot components, we separate hot orbits with a different λ_x to be prograde long-axis tubes ($\lambda_x > 0.25, |\lambda_z| \leq 0.25$), counter-rotating long-axis tubes ($\lambda_x < -0.25, |\lambda_z| \leq 0.25$), box orbits ($|\lambda_x| \leq 0.05, |\lambda_z| \leq 0.05$) and slowly-rotating orbits ($|\lambda_x|, |\lambda_z| \leq 0.25, |\lambda_x|$ or $|\lambda_z| > 0.05$).

Taking Fig. 7 into consideration, we find this galaxy is a prolate-like triaxial galaxy ($T \sim 0.7$). Examining the orbital separation as shown in Fig. 8, this galaxy has about 14 percent short-axis tube orbits (cold and warm components), 6 percent counter-rotating short-axis tubes, 17 percent long-axis tubes and 16 percent counter-rotating long-axis tubes. Neither rotation about the minor axis nor rotation about the major axis dominate this galaxy. These results are consistent with the model constraints shown in Fig. 2 and Fig. 3. The galaxy rotates slowly ($V \sim 20$ km/s compared to $\sigma \sim 130$ km/s), and there is a significant misalignment ($\Delta\text{PA} = |\text{PA}_{\text{kin}} - \text{PA}_{\text{pho}}| = 28^\circ$) between the kinematic position angle PA_{kin} and photometric position angle PA_{pho} . Such misalignments typically appear in the observation of triaxial galaxies.

6 STATISTICAL RESULTS

In this section, we show the composite statistical results from analysing all the central and satellite ETGs in our sample. We describe how we assess model uncertainties in § 6.1, mass distributions are presented in § 6.2, intrinsic stellar shapes in § 6.3, and orbit circularity distributions in § 6.4. In these sub-sections, we create the model determined galaxy parameter distributions by binning the parameter values using equal count bins. The parameter distributions, separated into central and satellite ETGs, are shown in Fig. 9, Fig. 11 and Fig. 12.

6.1 Model uncertainties

For an individual galaxy, the model uncertainties in our analysis have three components: a statistical uncertainty σ_{stat} , a systematic uncertainty σ_{sys} , and a systematic bias \mathcal{D} . The statistical uncertainty σ_{stat} is related to the confidence levels which are dominated by the model fluctuations as explained in § 4.2. For a given galaxy property X , we calculate its maximum value X_{max} , minimum value X_{min} and best-fitting value X_{best} in the models within a 1σ confidence level. Thus we define the statistical upper and lower errors as $\sigma_{\text{stat}+}(X) = X_{\text{max}} - X_{\text{best}}$ and $\sigma_{\text{stat}-}(X) = X_{\text{best}} - X_{\text{min}}$.

The systematic uncertainty σ_{sys} and systematic bias \mathcal{D} are evaluated based on the model tests against the Illustris simulations (Jin et al. 2019), as first introduced in § 2. We calculate the residuals of different galaxy properties between the model estimates and the true values for all mock data sets in Jin et al. (2019). The systematic uncertainty σ_{sys} represents the standard deviations of these residuals, while the systematic biases \mathcal{D} are the average values of the residuals. For a given galaxy property X , we calculate $\sigma_{\text{sys}}(X)$ and $\mathcal{D}(X)$ for oblate galaxies ($T_{\text{model}} \leq 0.3$), triaxial galaxies ($0.3 < T_{\text{model}} < 0.7$) and prolate galaxies ($T_{\text{model}} \geq 0.7$) separately, where T_{model} represents the triaxial parameter at one R_e found by the model. In Table 1, we list the values of $\sigma_{\text{sys}}(X)$ and $\mathcal{D}(X)$, with the exception of the systematic biases of the dark matter fractions as these depend on how close the NFW halo we used is to the real dark matter halo of a galaxy and are difficult to estimate (see Jin et al. 2019 for details).

For the average values of property X binned by N galaxies,

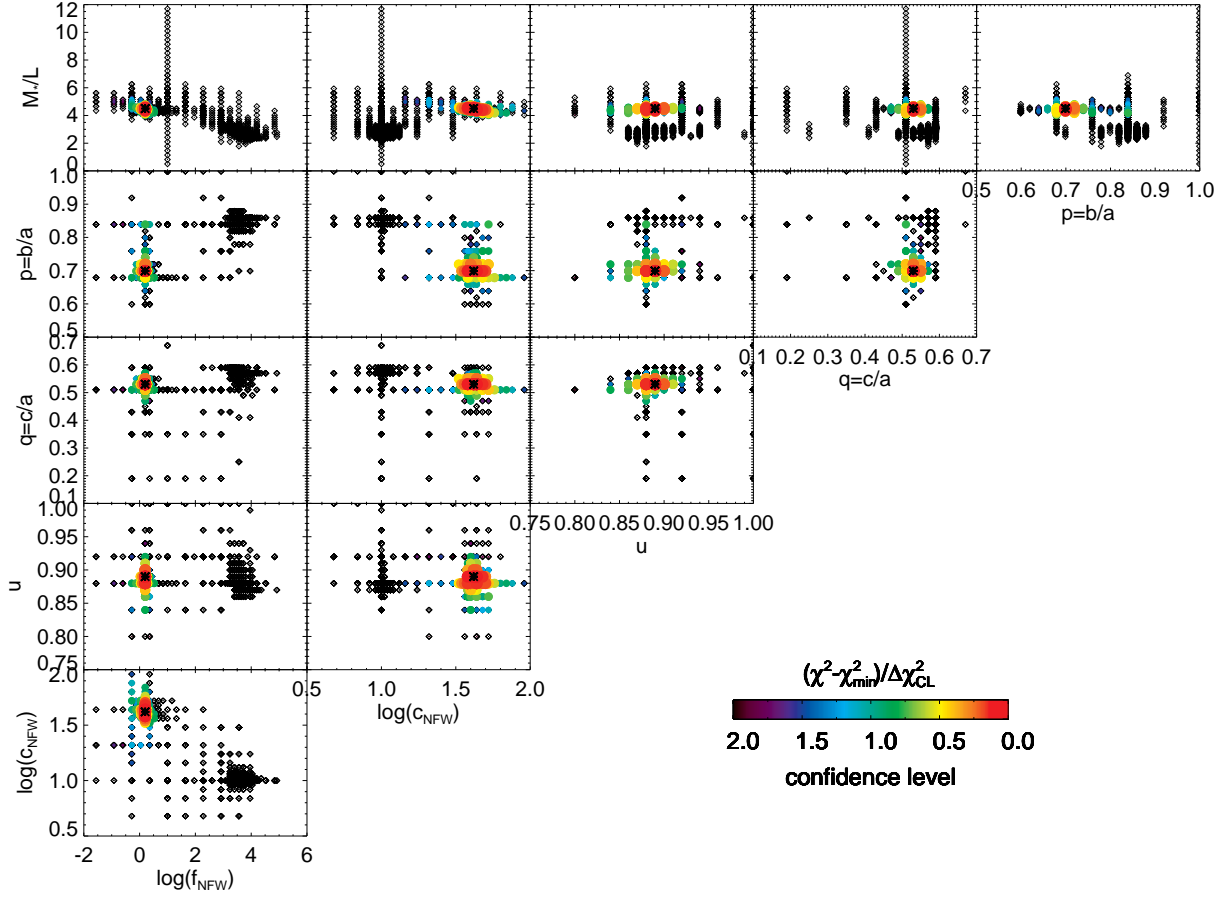


Figure 4. The parameter space of a complete set of modelling runs for galaxy 8247-6101. There are in total six free parameters: the stellar mass to light ratio M_*/L , the medium to major axis ratio $p = b/a$, the minor to major axis ratio $q = c/a$, the compression factor u , the dark matter concentration c_{NFW} and the virial mass in units of the total stellar mass $f_{\text{NFW}} = M_{200}/M_*$. The dots represent the parameters we have explored. The largest red dot with an asterisk inside indicates the best-fitting model and the other coloured dots indicate models within the 2σ confidence level, as indicated by the colour bar. The small black dots represent models outside of the 2σ confidence level (see § 4.2 for the definition of confidence level).

Table 1. The systematic uncertainties $\sigma_{\text{sys}}(X)$ and systematic biases $\mathcal{D}(X)$ for oblate, triaxial and prolate ETGs in Jin et al. (2019). From left to right, the properties are: (1) the dark matter fraction within one effective radius $f_{\text{DM}}(< R_e)$ (see § 6.2); (2) the triaxial parameter at one effective radius $T_e = (1 - p_e^2)/(1 - q_e^2)$ (see § 6.3); (3) the fractions of orbits f_{cold} , f_{warm} , f_{hot} and f_{CR} (see § 6.4); (4) the fractions of orbits f_{prolong} , f_{CRlong} , f_{box} and f_{SR} (see § 6.4). The systematic biases of dark matter fractions are hard to estimate, as they depend on how close the NFW halo we used is to the real dark matter halo of the galaxy (see Jin et al. 2019 for details).

$\sigma_{\text{sys}}(X)$		Property X									
		$f_{\text{DM}}(< R_e)$	T_e	f_{cold}	f_{warm}	f_{hot}	f_{CR}	f_{prolong}	f_{CRlong}	f_{box}	f_{SR}
Morphology	oblate	0.144	0.144	0.054	0.119	0.129	0.033	0.018	0.020	0.075	0.081
	triaxial	0.115	0.267	0.034	0.116	0.161	0.064	0.078	0.067	0.104	0.082
	prolate	0.099	0.187	0.018	0.071	0.095	0.051	0.100	0.098	0.168	0.085
$\mathcal{D}(X)$		Property X									
		$f_{\text{DM}}(< R_e)$	T_e	f_{cold}	f_{warm}	f_{hot}	f_{CR}	f_{prolong}	f_{CRlong}	f_{box}	f_{SR}
Morphology	oblate	/	0.023	0.022	0.101	-0.185	0.061	0.009	0.021	-0.084	-0.136
	triaxial	/	-0.003	-0.006	0.078	-0.129	0.056	0.036	0.031	-0.089	-0.116
	prolate	/	-0.014	0.014	0.043	-0.100	0.044	0.008	0.012	0.016	-0.149

we calculate their upper and lower overall uncertainties $U^+(X)$ and $U^-(X)$ as

$$U^+(X) = U_{\sigma}^+(X) + U_{\mathcal{D}}^+(X), \quad (4)$$

$$U^-(X) = U_{\sigma}^-(X) + U_{\mathcal{D}}^-(X), \quad (5)$$

where the terms with subscript σ represent the effect of the statis-

tical uncertainty $\sigma_{\text{stat}}(X)$ and the systematic uncertainty $\sigma_{\text{sys}}(X)$ to the overall model uncertainties, while the terms with subscript \mathcal{D} indicate the effect of the systematic bias $\mathcal{D}(X)$.

For the uncertainties caused by $\sigma_{\text{stat}}(X)$ and $\sigma_{\text{sys}}(X)$ in the mean value of property X in a bin of N galaxies, we have

$$U_{\sigma}^+(X) = \frac{1}{N} \sqrt{\sum_{n=1}^N [\sigma_{\text{stat}+}^2(X, n) + \sigma_{\text{sys}}^2(X, n)]}, \quad (6)$$

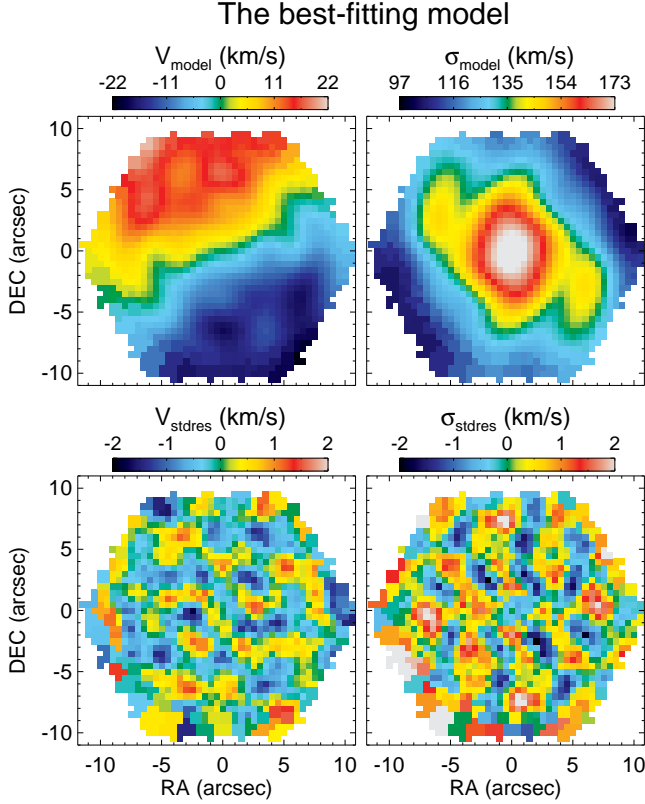


Figure 5. Kinematic data from the best-fitting model for galaxy 8247-6101 and related residual maps. The first row shows the mean velocity V_{model} and velocity dispersion σ_{model} maps, while the second row shows the corresponding standardized residual maps between the model and observational data: $V_{\text{stdres}} = (V_{\text{model}} - V_{\text{obs}})/V_{\text{obserr}}$ and $\sigma_{\text{stdres}} = (\sigma_{\text{model}} - \sigma_{\text{obs}})/\sigma_{\text{obserr}}$.

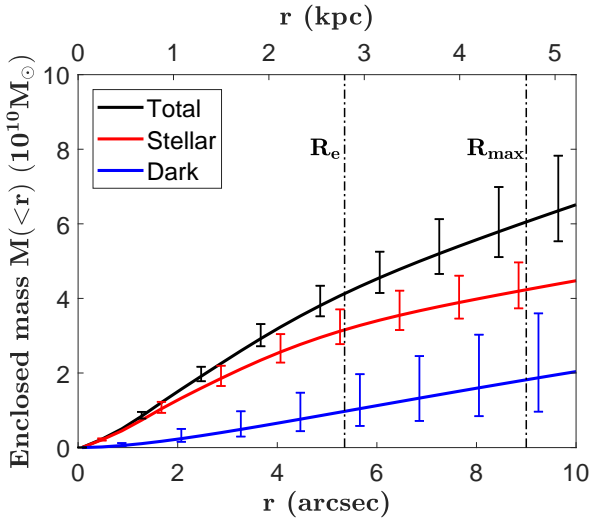


Figure 6. Mass profiles for the example galaxy 8247-6101 inferred from Schwarzschild modelling. The black curve indicates the mass profile, while the red and blue curves represent stellar mass and dark matter respectively. The error bars represent the 1σ confidence levels. The vertical dashed lines show the effective radius R_e and the maximum IFU coverage R_{max} .

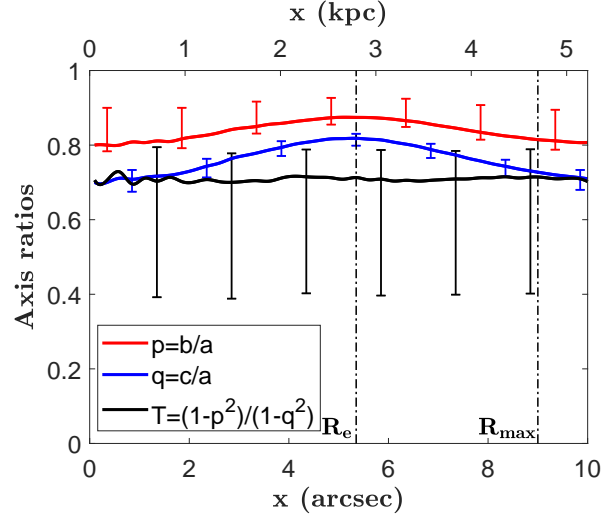


Figure 7. Variation along the major axis (x) of the axial ratios $p = b/a$, $q = c/a$ and triaxial parameter $T = (1 - p^2)/(1 - q^2)$ for the example galaxy 8247-6101. The red, blue and black curves correspond to p , q and T . The error bars represent the 1σ confidence levels. The vertical dashed lines indicate the effective radius R_e and the maximum IFU coverage R_{max} .

$$U_{\sigma}^{-}(X) = \frac{1}{N} \sqrt{\sum_{n=1}^N [\sigma_{\text{stat}}^2(X, n) + \sigma_{\text{sys}}^2(X, n)]}, \quad (7)$$

where n represents the n -th galaxy in the bin.

We consider the effect of systematic bias $\mathcal{D}(X)$ according to its sign. For a bin of N galaxies, we have

$$\begin{cases} U_{\mathcal{D}}^{+}(X) = -\overline{\mathcal{D}}(X, n) \\ U_{\mathcal{D}}^{-}(X) = 0 \end{cases} \quad \text{if } \overline{\mathcal{D}}(X, n) < 0, \quad (8)$$

and

$$\begin{cases} U_{\mathcal{D}}^{+}(X) = 0 \\ U_{\mathcal{D}}^{-}(X) = \overline{\mathcal{D}}(X, n) \end{cases} \quad \text{if } \overline{\mathcal{D}}(X, n) > 0, \quad (9)$$

with

$$\overline{\mathcal{D}}(X, n) = \frac{1}{N} \sum_{n=1}^N \mathcal{D}(X, n). \quad (10)$$

This means that any underestimations in the simulation tests result in a larger upper error bar, as we expect the real values of the property to be larger than our model predictions, while any overestimations, correspondingly, cause a larger lower error bar. The mock galaxies we used in (Jin et al. 2019) are generally representative of real observations, so we expect that the method works similarly with the two samples and has an equivalent systematic bias. However, it is difficult to match our real galaxies to mock galaxies one-to-one, and we therefore use the arithmetic mean of biases in this work.

The overall uncertainties $U^{+}(X)$ and $U^{-}(X)$ are treated as error bars in the figures plotted in § 6.2, § 6.3 and § 6.4.

6.2 Mass distributions

The total mass distributions M_{tot} in our investigations include a stellar component M_{*}^{Schw} and a dark matter component M_{dark} (the

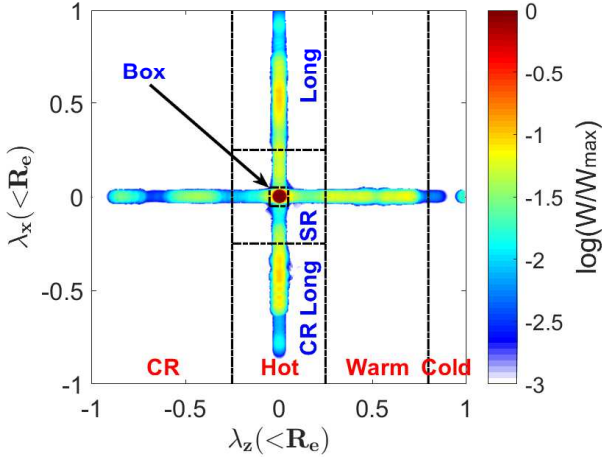


Figure 8. Binned orbit weights by classification within one R_e on the $\lambda_z - \lambda_x$ plane for galaxy 8247-6101. The binned values, $\log(W_j/W_{\max})$, are indicated by the colour bar. W_j is the total orbit weight in λ_z vs λ_x bin j , and W_{\max} is the maximum of the W_j . The black dashed lines show the classification of orbits into different categories. Orbits with different λ_z values range from cold ($\lambda_z \geq 0.8$), warm ($0.25 < \lambda_z < 0.8$), hot ($-0.25 \leq \lambda_z \leq 0.25$) and counter-rotating orbits ($\lambda_z < -0.25$). Hot orbits are separated into four components: prograde long-axis tubes ($\lambda_x > 0.25, |\lambda_z| \leq 0.25$), counter-rotating long-axis tubes ($\lambda_x < -0.25, |\lambda_z| \leq 0.25$), box orbits ($|\lambda_x| \leq 0.05, |\lambda_z| \leq 0.05$) and slowly-rotating orbits ($|\lambda_x|, |\lambda_z| \leq 0.25, |\lambda_x|$ or $|\lambda_z| > 0.05$). Note that the divisions of long-axis tubes and box orbits are just approximations and not the exact.

mass of a black hole is very small by comparison). We calculate the dark matter fraction within one effective radius $f_{\text{DM}}(< R_e) = M_{\text{dark}}/M_{\text{tot}}$. Fig. 9 shows the relationship between the dark matter fraction $f_{\text{DM}}(< R_e)$ and the population synthesis total stellar mass $\log(M_*/M_\odot)$. The red asterisks represent central ETGs while the blue asterisks represent satellite ETGs. The coloured solid lines show the mean binned values and their uncertainties. We can clearly see the dark matter fraction increases with the stellar mass and there is no difference between central and satellite ETGs in the same mass range. Most galaxies around $10^{10.5} M_\odot$ have $f_{\text{DM}}(< R_e) < 0.2$, while a lot of massive galaxies with $11.0 < \log(M_*/M_\odot) < 11.5$ have $f_{\text{DM}}(< R_e) > 0.4$. This trend is generally consistent with Cappellari et al. (2013a) who used Jeans Anisotropic Modelling (JAM) for ATLAS^{3D} ETGs and found $f_{\text{DM}}(< R_e)$ increases with stellar mass when $\log(M_*/M_\odot) > 10.6$. However, their dark matter fractions are lower than our results for massive galaxies with $f_{\text{DM}}(< R_e) \sim 0.3$ when using fixed NFW halo based on Moster et al. (2010) and $f_{\text{DM}}(< R_e) \sim 0.2$ when using free NFW halo. The most massive ETGs are mainly slowly rotating triaxial or prolate galaxies, which do not match the assumptions within JAM modelling very well. In addition, the true dark matter profiles may deviate from NFW profiles. We discuss possible biases for dark matter fractions due to different model assumptions in § 8.

6.3 Intrinsic stellar shapes

The stellar component in our modelling is taken to be triaxial. As described earlier and in Jin et al. (2019), we use three parameters to indicate the intrinsic stellar shapes, the medium to long axis ratio $p = b/a$, the short to long axis ratio $q = c/a$ and the major axis

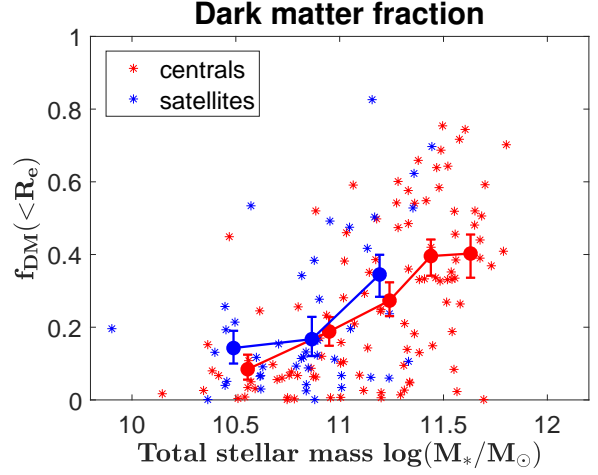


Figure 9. The dark matter fraction within one R_e as a function of the galaxies' total stellar mass M_* . The red asterisks represent central ETGs while the blue asterisks, satellite ETGs. The red and blue solid lines with error bars show the mean binned values and their uncertainties calculated based on § 6.1. Here we only consider the statistical errors σ_{stat} and systematic errors σ_{sys} since the systematic bias \mathcal{D} is hard to evaluate as the true dark matter density slope is not known (see Jin et al. 2019 for details).

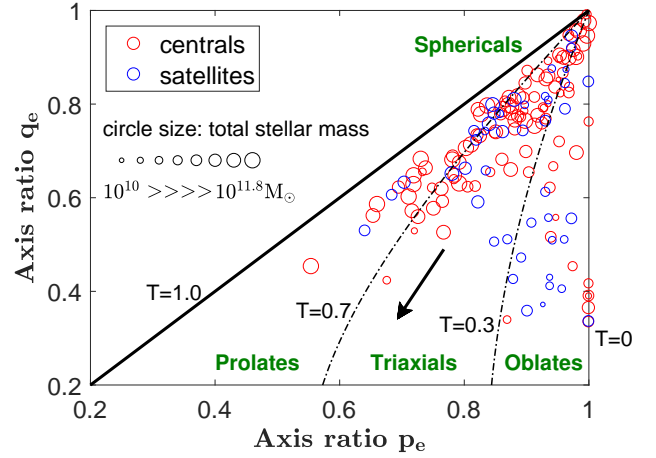


Figure 10. The distribution of axis ratios p_e versus q_e at one R_e from the best-fitting models for all galaxies in our sample. The red circles represent central ETGs while the blue circles represent satellite ETGs. The black dashed curves from right to left indicate $T_e = 0.3$, $T_e = 0.7$ and the black thick line is for $T_e = 1.0$. Larger circle sizes indicate higher total stellar mass. The black arrow indicates the average overestimations $\Delta p_e = 0.07$ and $\Delta q_e = 0.14$ according to tests using the Illustris simulations (Jin et al. 2019).

compression factor $u = a_{2D}/a_{3D}$ ($u \leq 1$), where a_{3D} is the typical scale of a three-dimensional Gaussian (the standard deviation along major axis) and a_{2D} is the corresponding typical scale of projected two-dimensional Gaussian. Here we concentrate on p and q as they are directly related to galaxy morphologies. For each galaxy, we obtain the average axis ratio and triaxial parameter profiles as shown in Fig. 7. We take p_e, q_e and $T_e = (1 - p_e^2)/(1 - q_e^2)$ at one effective radius for statistical analysis.

Fig. 10 shows the distribution of axis ratios p_e versus q_e for all

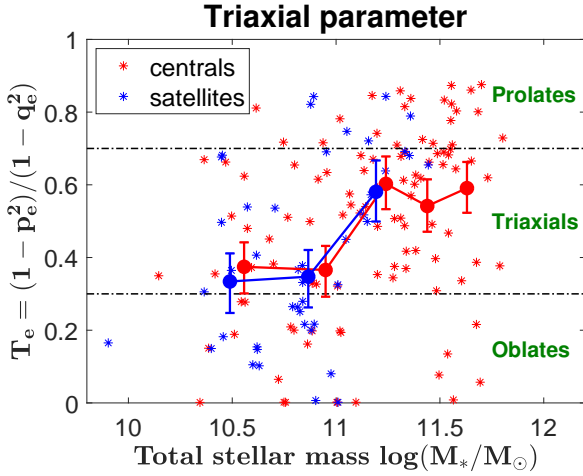


Figure 11. The variation of the triaxial parameter $T_e = (1 - p_e^2)/(1 - q_e^2)$ as a function of total stellar mass. The red asterisks represent central ETGs while the blue asterisks represent satellite ETGs. The coloured solid lines show the mean binned values and their uncertainties, including the effect of statistical uncertainties, systematic uncertainties and systematic biases as in equations (4) to (10). The horizontal dashed lines indicate $T_e = 0.3$ and $T_e = 0.7$.

galaxies. The red circles represent central ETGs while the blue circles represent satellite ETGs, and the larger symbol sizes indicate larger total stellar masses for the galaxies. The black dashed curves separate the galaxies into oblates ($T_e \leq 0.3$), triaxials ($0.3 < T_e < 0.7$) and prolates ($T_e \geq 0.7$). The black arrow indicates the average overestimation of p and q in our simulation tests (Jin et al. 2019). We suggest that there should not be so many galaxies that are close to spherical ($p \sim 1$ and $q \sim 1$). We see that large circles (high stellar masses) tend to be located in the prolate regions while the small circles (low stellar masses) tend to be located in the oblate regions. In order to check the variation of intrinsic stellar shapes as a function of stellar mass quantitatively, we show the triaxial parameter T_e as a function of total stellar mass M_* in Fig. 11. The red asterisks represent central ETGs while the blue asterisks represent satellite ETGs. The coloured solid lines show the mean binned values and their uncertainties including the effects of statistical uncertainties, systematic uncertainties and systematic biases as in equations (4) to (10). Lower mass galaxies are more oblate-like with their average triaxial parameter $T_e \sim 0.4$, while higher mass galaxies are more prolate-like with $T_e \sim 0.6$. There is a rapid change around $\log(M_*/M_\odot) = 11.1$. Both central and satellite ETGs show similar variations of T_e as a function of stellar mass M_* . The triaxial parameters of central and satellite ETGs are consistent with each other within the 1σ error bar at the same stellar mass.

6.4 Orbit circularity distributions

We use the orbit circularity distributions $f(\lambda_z)$ and $f(\lambda_x)$ to illustrate what the internal orbital structures of our galaxies might be like. As shown in Fig. 8, for each galaxy, we obtain the probability density of orbits within one R_e and separate them into different components on the $\lambda_z - \lambda_x$ plane. We calculate the luminosity weighted fraction of each component within one R_e .

Fig. 12 shows the fractions of cold ($f_{\text{cold}}, \lambda_z \geq 0.8$), warm ($f_{\text{warm}}, 0.25 < \lambda_z < 0.8$), hot ($f_{\text{hot}}, -0.25 \leq \lambda_z \leq 0.25$) and counter-rotating orbits ($f_{\text{CR}}, \lambda_z < -0.25$) versus the total stel-

lar mass. The symbols have the same meaning as Fig. 11. When the stellar mass increases, f_{cold} and f_{warm} decrease while f_{hot} increases. We find that these three fractions all have rapid changes around $\log(M_*/M_\odot) = 11.1$. Galaxies with $\log(M_*/M_\odot) < 11.1$ have on average $f_{\text{cold}} \sim 0.1$, $f_{\text{warm}} \sim 0.35$ and $f_{\text{hot}} \sim 0.45$, while galaxies with $\log(M_*/M_\odot) > 11.1$ have on average $f_{\text{cold}} \sim 0.05$, $f_{\text{warm}} \sim 0.2$ and $f_{\text{hot}} \sim 0.65$. The counter-rotating component generally contributes less than a fraction of 0.1 and varies little as a function of M_* . The variations of f_{cold} , f_{warm} , f_{hot} and f_{CR} generally have similar trend as the CALIFA ETGs (Zhu et al. 2018b). However, there are significant differences due to the different selection functions of the two samples. We show the comparison of our results and CALIFA results in the appendix.

Following Jin et al. (2019), we divide the hot component into prograde long-axis tubes ($f_{\text{prolong}}, \lambda_x > 0.25, |\lambda_z| \leq 0.25$), counter-rotating long-axis tubes ($f_{\text{CRlong}}, \lambda_x < -0.25, |\lambda_z| \leq 0.25$), box orbits ($f_{\text{box}}, |\lambda_x| \leq 0.05, |\lambda_z| \leq 0.05$) and slowly-rotating orbits ($f_{\text{SR}}, |\lambda_x|, |\lambda_z| \leq 0.25, |\lambda_x|$ or $|\lambda_z| > 0.05$). The variations of these four components as a function of total stellar mass are shown in Fig. 13 and the symbols are the same as Fig. 11. We can see f_{prolong} , f_{CRlong} , f_{box} and f_{SR} all increase with increasing stellar mass. There is also a rapid change around $\log(M_*/M_\odot) = 11.1$ as revealed in Fig. 12.

Combining Figs. 12 and 13, galaxies more massive than $10^{11.1} M_\odot$ have a significant fraction of box orbits ($f_{\text{box}} \sim 0.3$ on average) with centrophilic orbits dominating. However, these galaxies are mainly constructed by tube orbits, with similar amounts of short-axis tube orbits ($f_{\text{cold}} + f_{\text{warm}} + f_{\text{CR}} \sim 0.35$) and long-axis tube orbits ($f_{\text{prolong}} + f_{\text{CRlong}} \sim 0.25$). The fraction of counter-rotating orbits ($f_{\text{CR}} + f_{\text{CRlong}} \sim 0.25$) are almost comparable to the co-rotating tube orbits ($f_{\text{cold}} + f_{\text{warm}} + f_{\text{prolong}} \sim 0.4$), thus these galaxies have little net rotation. Galaxies less massive than $10^{11.1} M_\odot$ are usually dominated by short-axis tube orbits ($f_{\text{cold}} + f_{\text{warm}} + f_{\text{CR}} \sim 0.55$), and have less long-axis tube orbits ($f_{\text{prolong}} + f_{\text{CRlong}} \sim 0.15$) and centrophilic box orbits ($f_{\text{box}} \sim 0.3$), at the same time, counter-rotating orbits ($f_{\text{CR}} + f_{\text{CRlong}} \sim 0.15$) are not remarkable compared to the co-rotating tube orbits ($f_{\text{cold}} + f_{\text{warm}} + f_{\text{prolong}} \sim 0.55$), thus these galaxies usually show significant net rotation around the short axis. Not forgetting that orbit distributions are at best only indicative, due to the complicated select function of the MaNGA sample, the orbit distributions of ETGs we obtained here are not generally representative quantitatively of the ETGs in the nearby universe. In both figures, there are no significant differences between central and satellite ETGs regardless of the total stellar mass involved. Since the orbit structures are directly related with galaxy morphologies, it is not surprising that we find similar trends in § 6.3 and § 6.4.

7 THE EFFECT OF LOCAL ENVIRONMENT

As indicated in section § 2, we investigate the environmental influence on internal galaxy properties by introducing galaxy neighbour counts $N_{\text{neighbour}}(< r_p)$, which gives the number of galaxies around a galaxy within a projected radius r_p (Li et al. 2008), using a complete photometric reference sample of nearby star-forming galaxies constructed from the New York University Value-Added Galaxy Catalog (NYU-VAGC, Blanton et al. 2005b). Neighbours are counted in the vicinity of our galaxies and a statistical correction is applied to remove the effect of chance projections by subtracting the average counts around randomly placed galaxies (Li et al. 2008). In this section, we study the variation of

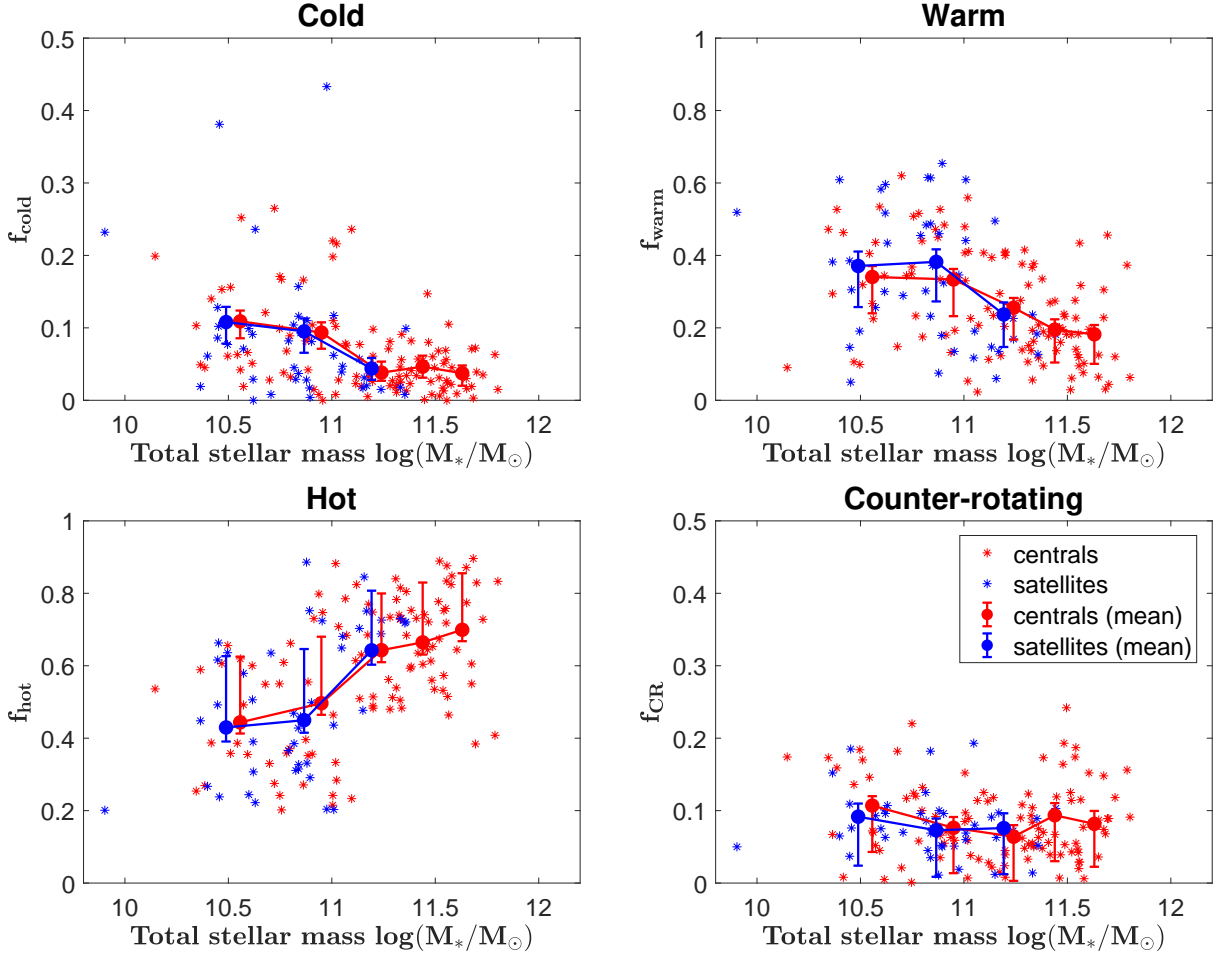


Figure 12. The luminosity fractions of cold, warm, hot and counter-rotating orbits versus total stellar mass. From top-left to bottom-right, they are: cold ($\lambda_z \geq 0.8$), warm ($0.25 < \lambda_z < 0.8$), hot ($-0.25 \leq \lambda_z \leq 0.25$) and counter-rotating ($\lambda_z < -0.25$) components. The red asterisks represent central ETGs while the blue asterisks, satellite ETGs. The coloured solid lines show the mean binned values and their uncertainties, including the effects of statistical uncertainties, systematic uncertainties and systematic biases as in equations (4) to (10).

$N_{\text{neighbour}}(< r_p)$ for galaxies separated into different groups based on two of their internal properties namely the hot orbit fraction f_{hot} and the triaxial parameter T_e at effective radius R_e .

Due to the rapid change of intrinsic structures at $M_* \sim 10^{11.1} M_\odot$, we first separate galaxies into low-mass ($M_* < 10^{11.1} M_\odot$) and high-mass ($M_* > 10^{11.1} M_\odot$) ETGs. Then for low-mass and high-mass ETGs separately, we perform a linear fit of f_{hot} as a function of stellar mass. The fitted values roughly represent the average $\overline{f_{\text{hot}}}$ at different stellar mass $\log(M_*/M_\odot)$. The low-mass ETGs ($M_* < 10^{11.1} M_\odot$) are then divided into two groups: (1) A1, $f_{\text{hot}} < \overline{f_{\text{hot}}}$; (2) B1, $f_{\text{hot}} > \overline{f_{\text{hot}}}$. Similarly for high-mass ETGs ($M_* > 10^{11.1} M_\odot$), we also have two groups: (1) C1, $f_{\text{hot}} < \overline{f_{\text{hot}}}$; (2) D1, $f_{\text{hot}} > \overline{f_{\text{hot}}}$. A1 and B1 will be a comparison pair with, their major difference being the hot orbit fraction f_{hot} for similar stellar mass. Similarly C1 and D1 will be another pair.

We calculate the neighbour counts for each group of galaxies $N_{\text{neighbour}}(< r_p)$ as a function of projected radius r_p , using SDSS galaxies with r-band magnitude $M_r < -20$ as the photometric reference sample. We perform the calculation several times using bootstrapping, and the variations from the bootstrapping results are used as errors. In Fig. 14, we show the comparison between A1 and B1 on the left, and C1 and D1 on the right. The top panels show the variation of $N_{\text{neighbour}}(< r_p)$ as a function of r_p for different

groups, the middle panels represent the ratios of $N_{\text{neighbour}}$ between the corresponding two groups, while the bottom panels are their $g-i$ colour distributions. A1 and B1 have similar stellar mass and $g-i$ colour distribution, while the one with a higher hot orbit fraction (B1) has a higher $N_{\text{neighbour}}$ at $r_p \sim 40$ kpc. Similarly, C1 and D1 have similar stellar mass and $g-i$ colour distribution, and the one with a higher hot orbit fraction (D1) has a higher $N_{\text{neighbour}}$ at $r_p \sim 40$ kpc. The corresponding ratios are $N_{A1}/N_{B1} \sim 0.3$ and $N_{C1}/N_{D1} \sim 0.3$, although there are still relatively large uncertainties.

A similar separation is performed based on the triaxiality T_e . We estimate the average triaxiality $\overline{T_e}$ as a function of stellar mass $\log(M_*/M_\odot)$ for low-mass and high-mass ETGs separately. We then divide low-mass ETGs ($M_* < 10^{11.1} M_\odot$) into two groups: (1) A2, $T_e < \overline{T_e}$; (2) B2, $T_e > \overline{T_e}$; and similarly divide high-mass ETGs ($M_* > 10^{11.1} M_\odot$) into two groups: (1) C2, $T_e < \overline{T_e}$; (2) D2, $T_e > \overline{T_e}$. A2 and B2 will be a comparison pair and, their major difference is the triaxiality T_e for similar stellar mass. Similarly C2 and D2 will be another pair.

We calculate $N_{\text{neighbour}}(< r_p)$ as a function of projected radius r_p for different groups as shown in Fig. 15. A2 and B2 have similar mass and $g-i$ colour distribution. The one with higher T_e (B2) has higher $N_{\text{neighbour}}$ at $r_p \sim 40$ kpc with the ratio $N_{A2}/N_{B2} \sim 0.03$.

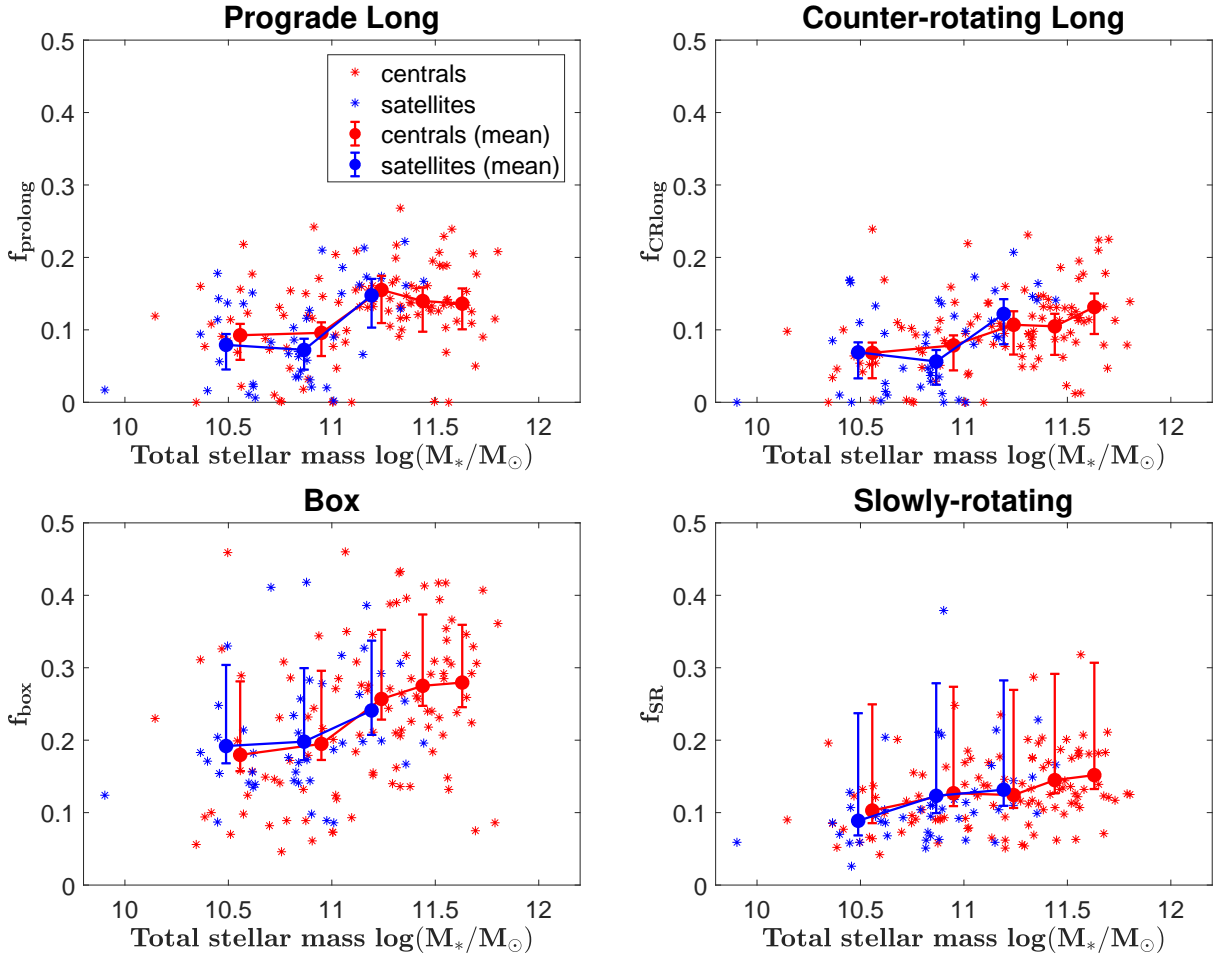


Figure 13. The luminosity fractions of long-axis tubes, box orbits and slowly-rotating orbits versus total stellar mass. From top-left to bottom-right, they are: prograde long-axis tube ($\lambda_x > 0.25, |\lambda_z| \leq 0.25$), counter-rotating long-axis tube ($\lambda_x < -0.25, |\lambda_z| \leq 0.25$), box ($|\lambda_x| \leq 0.05, |\lambda_z| \leq 0.05$) and slowly-rotating ($|\lambda_x|, |\lambda_z| \leq 0.25, |\lambda_x|$ or $|\lambda_z| > 0.05$) components. The symbols and lines have the same meaning as those in Fig. 12. Note that the divisions of long-axis tubes and box orbits are just approximations and not the exact.

C2 and D2 have similar mass and $g-i$ colour distribution. We also find that the one with higher T_e (D2) has higher $N_{\text{neighbour}}$ at $r_p \sim 40$ kpc. With the ratio $N_{C2}/N_{D2} \sim 0.3$, the difference within this pair is not as significant as the pair of A2 and B2.

The above analysis shows that galaxies with more close neighbours ($r_p \sim 40$ kpc) tend to be more prolate-like and have more hot orbits. For similar stellar mass and colour distributions for each pair, the differences in the internal structures are unlikely to be caused by their star formation histories. It indicates that close neighbours may affect the internal structures (even in the inner $1 R_e$ regions) of ETGs. Although our sample is relatively small, and the uncertainties are large, we see that the comparison of the four pairs (A1 vs B1, C1 vs D1, A2 vs B2 and C2 vs D2) lead to coherent results.

Our model uncertainties could contribute part of the variations on T_e and f_{hot} , which could cause the mixture of galaxies in the two groups, separated by an average value of T_e and f_{hot} in each pair, thus diluting the differences. The intrinsic differences of $N_{\text{neighbour}}$ for the two groups of galaxies in each pair could be larger.

8 DISCUSSION

Fig. 9 shows that our dark matter fractions within one effective radius $f_{\text{DM}}(< R_e) = M_{\text{dark}}/M_{\text{tot}}$ obtained from Schwarzschild modelling are $f_{\text{DM}}(< R_e) \sim 0.4$ on average for massive ETGs, which is typically higher than the JAM results (Cappellari et al. 2013a). Most massive ETGs are slow rotators and are usually not oblate-like, so the assumptions required for oblate JAM modelling are not met for the dynamical modelling of these galaxies, which means there could be some unphysical biases. Our triaxial Schwarzschild modelling is much more free and does not have this problem. According to our model tests with mock data created from the Illustris simulations (Jin et al. 2019), when the estimations of total masses are accurate, $f_{\text{DM}}(< R_e)$ could be overestimated by a factor of ~ 38 percent if the galaxies have cored dark matter haloes and we model assuming the galaxies should follow the NFW profile. When we use a generalized NFW (gNFW, Cappellari et al. 2013a) halo instead, the overestimation can be reduced to ~ 18 percent. For real MaNGA galaxies, we do not know the true dark matter profiles, and so assume NFW haloes in our models. Thus $f_{\text{DM}}(< R_e)$ could be overestimated with an upper limit of ~ 38 percent. Cappellari et al. (2013a) used both fixed and free NFW haloes in their JAM modelling, and they gave lower $f_{\text{DM}}(< R_e)$ values than ours for massive

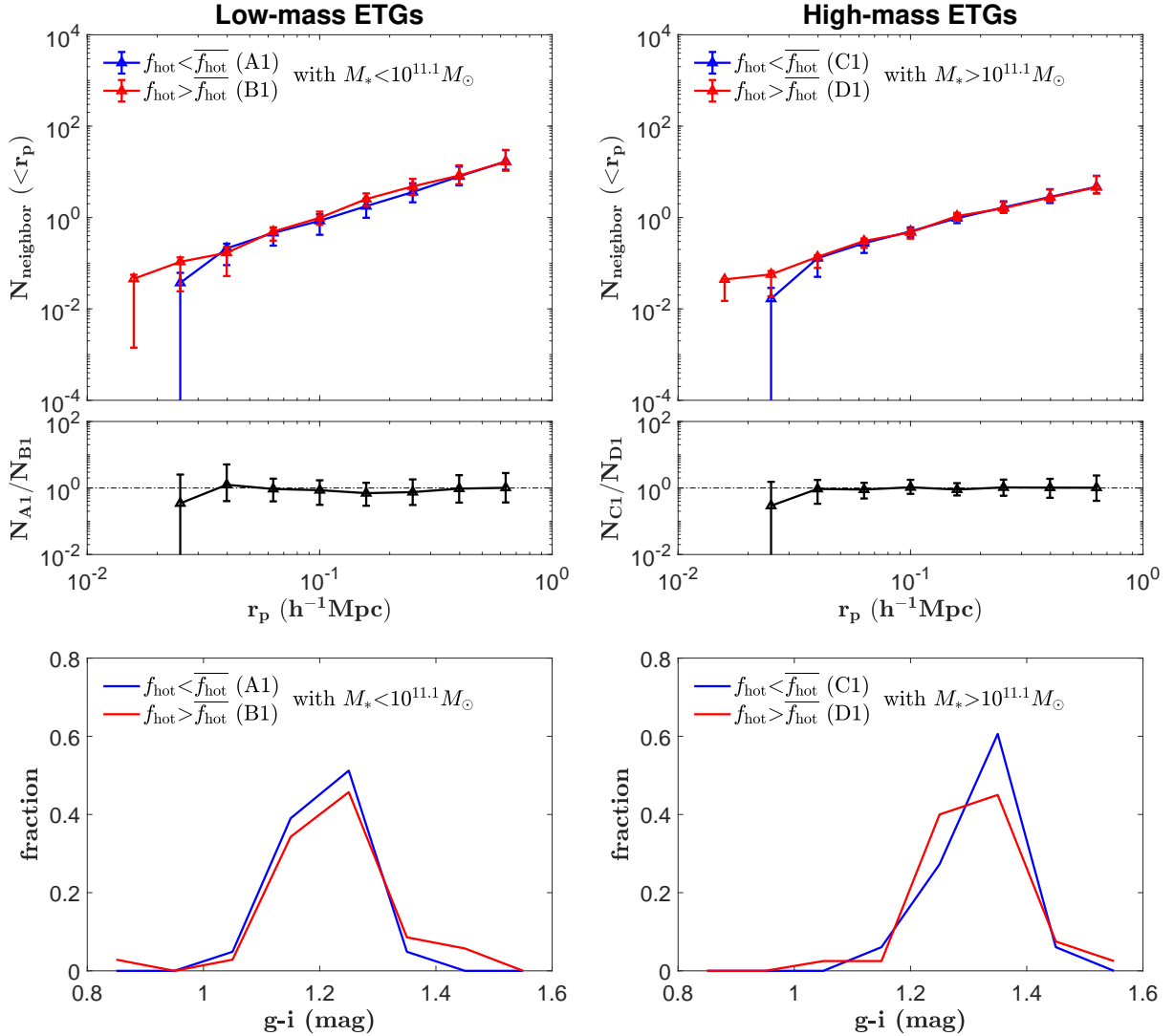


Figure 14. The neighbour counts $N_{\text{neighbour}}(<r_p)$ as a function of projected radius r_p and the colour distribution of $g-i$ for four different groups of galaxies separated as follows: A1, $M_* < 10^{11.1} M_\odot$ and $f_{\text{hot}} < \overline{f_{\text{hot}}}$; B1, $M_* < 10^{11.1} M_\odot$ and $f_{\text{hot}} > \overline{f_{\text{hot}}}$; C1, $M_* > 10^{11.1} M_\odot$ and $f_{\text{hot}} < \overline{f_{\text{hot}}}$; and D1, $M_* > 10^{11.1} M_\odot$ and $f_{\text{hot}} > \overline{f_{\text{hot}}}$. We compare A1 and B1 as a pair on the left and C1 and D1 as another pair on the right panels. The upper panels show the variation of $N_{\text{neighbour}}(<r_p)$ with r_p for each group of galaxies. In the middle, the black lines with error bars represent the ratios of neighbour counts between two groups in each pair. The bottom panels show the corresponding normalized $g-i$ colour distribution.

galaxies on average. If the true dark matter profiles of these massive ETGs profile are cored, we could have overestimated the dark matter fractions, and the results from JAM might then be less biased. Although this inconsistency between the two different modelling methods exists, our main conclusions about dark matter fractions and orbital structures are not affected.

In § 6.2 and § 6.3, we find a rapid change around $\log(M_*/M_\odot) \sim 11.1$ which divides galaxies into two categories. Low-mass ETGs with $\log(M_*/M_\odot) < 11.1$ tend to be oblate-like and dominated by rotation about the minor axis, while high-mass ETGs with $\log(M_*/M_\odot) > 11.1$ tend to be prolate-like and dominated by rotation about the major axis and centrophilic orbits. A similar rapid change also exists in Fig. 9. These trends in the inner parts of ETGs are generally consistent with the two formation paths of ETGs proposed by Cappellari (2016). Slow rotators grow via mergers, are triaxial and dominate the massive region. By comparison, low-mass fast rotators grow via gas accretion and their structure parallels that of spiral galaxies. The increasing fractions

of long-axis tube orbits with stellar mass support the scenario that the most massive slow-rotators could form via major dry mergers (Li et al. 2018). Detailed comparison of the orbit distributions between these MaNGA galaxies and cosmologically simulated galaxies could possibly lead to a more quantitative understanding of the formation history.

As alluded to in § 1, the orbit circularity distributions in § 6.4 being based on only partially constrained, 6-dimensional phase space model data must not be taken as a true representation of a real galaxy. The distributions may be taken however as illustrative or indicative of what the structures might look. In addition, it must be remembered that Schwarzschild’s method can only weight the orbits it is given. Changing the given orbits will change the orbits selected by the modelling process, and have an impact on the orbit circularity distribution.

We find no difference on mass distributions, intrinsic stellar shapes and internal orbital structures for central and satellite ETGs in the same mass range. This result is consistent with Greene et al.

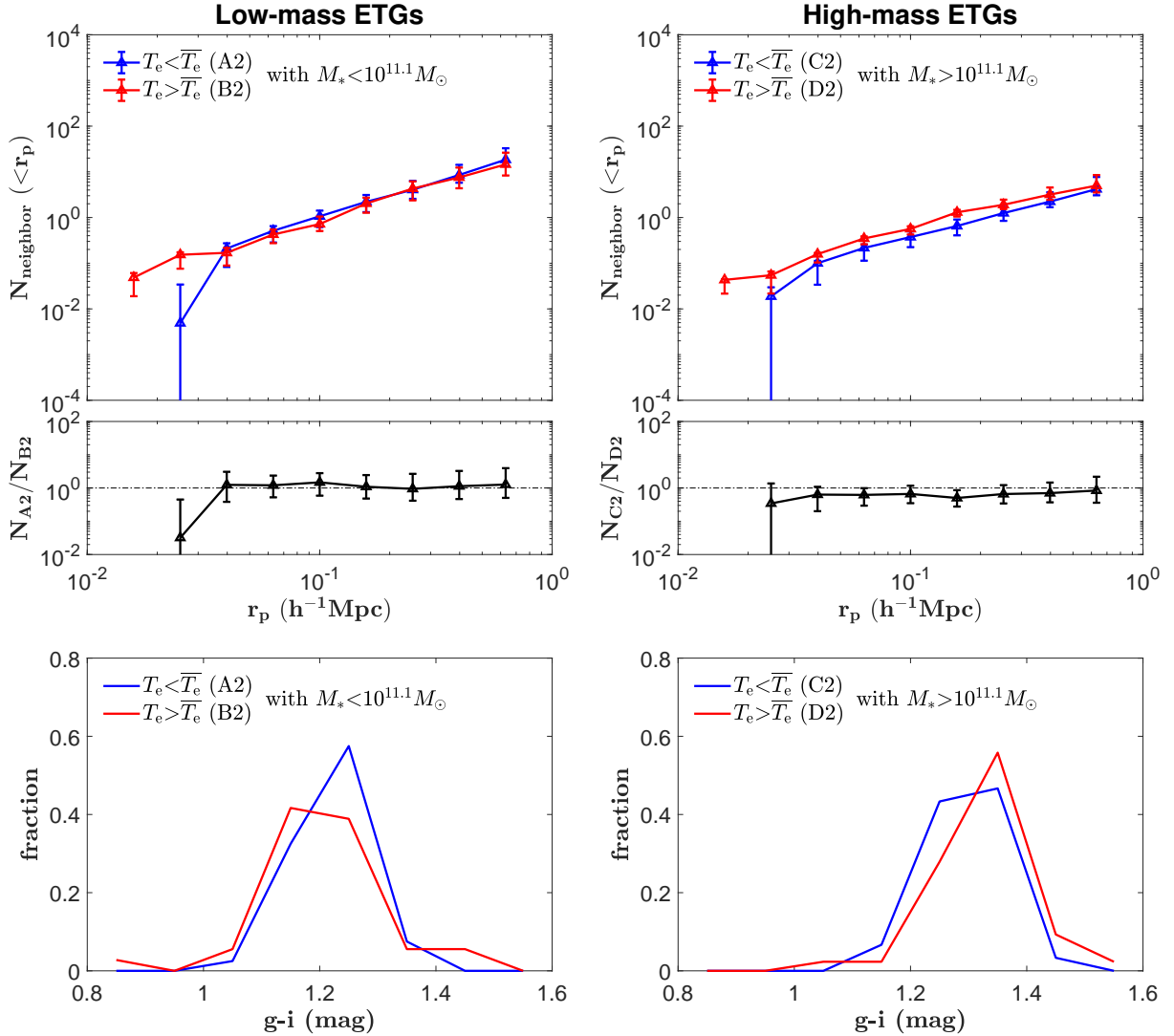


Figure 15. Similarly to Fig. 14, but four groups separated based on triaxial parameter $T_e = \overline{T_e}$: A2, $M_* < 10^{11.1} M_\odot$ and $T_e < \overline{T_e}$; B2, $M_* < 10^{11.1} M_\odot$ and $T_e > \overline{T_e}$; C2, $M_* > 10^{11.1} M_\odot$ and $T_e < \overline{T_e}$; and D2, $M_* > 10^{11.1} M_\odot$ and $T_e > \overline{T_e}$.

(2018), who used two-dimensional kinematics to investigate the difference between central and satellite ETGs. The internal structures of galaxies are dominated by the rapid physical processes associated with the growth of stellar mass. The physical processes due to the difference between centrals and satellites are unlikely to affect galaxy structures, especially in the inner regions ($< R_e$). However, when considering the local density environments indicated by neighbour counts, we find that galaxies that have higher neighbour counts within ~ 40 kpc tend to be more prolate-like and have more hot orbits. There is evidence that prolate galaxies are likely originated from major mergers (Tsatsi, et al. 2017; Li et al. 2018). The increasing fractions of both prograde and counter-rotating long-axis tube orbits with stellar mass as shown in Fig. 13 also support this statement. There is no clear evidence whether or not minor mergers or tidal forces from nearby galaxies can affect the stellar orbit distributions of massive ETGs in the inner regions ($< R_e$). Our results suggest that the $N_{\text{neighbour}}$ might be an indicator of galaxies' merger histories. A galaxy with more close neighbours today indicates a denser environment, and this galaxy may have had a higher frequency of major mergers in the past.

All the analysis we have performed has been undertaken using SPS stellar masses to analyse galaxy features or properties determined from dynamical modelling. We therefore have had to deal with analysis using data from different modelling regimes. Using SPS stellar masses where there is no other option, for example in utilising existing MaNGA or SDSS catalogues, is understandable. Dynamical masses, both stellar and dark matter, come as a pair in the sense that there is a degeneracy between them that is not resolvable with the galaxy observations that are currently available. Both Li et al. (2016) and Jin et al. (2019) make the point however that the total mass is recovered well. Thus, there is no good reason to discard dynamical stellar masses for SPS masses when calculating dark matter fractions. Similarly, orbits and values derived from them are related to the total mass in a galaxy. Why researchers choose to ignore total mass and just analyse orbits with respect to stellar mass is unclear, and why an SPS mass is sometimes substituted for a dynamical stellar mass is even less clear. It may be that uncertainties about a galaxy's dark matter distribution are considered to be “large” with an associated effect on the stellar distribution. Switching to an SPS stellar mass will not resolve the issues

with the dark matter distribution. What we have highlighted here is that cross-overs between modelling regimes needs to be justified and communicated effectively. We will continue to progress this in the future.

9 SUMMARY

We have met the objectives we set out in § 1 in that we have

- (i) modelled the selected MaNGA early-type galaxies individually using Schwarzschild’s method and determined their mass distributions, intrinsic stellar shapes and internal orbit distributions,
- (ii) examined statistically the differences and similarities between central and satellite ETGs, and
- (iii) assessed the role of the environment in the galaxies’ evolution.

We set out more detail on our findings below. Significantly we find the intrinsic properties of ETGs have a rapid change at about $\log(M_*/M_\odot) \sim 11.1$.

- Dark matter fractions within one effective radii $f_{\text{DM}}(< R_e)$ increase with total stellar mass for our sample. Low-mass ETGs ($\log(M_*/M_\odot) < 11.1$) have on average $f_{\text{DM}}(< R_e) \sim 0.2$ and high-mass ETGs ($\log(M_*/M_\odot) > 11.1$) have on average $f_{\text{DM}}(< R_e) \sim 0.4$.
- The stellar components of low-mass ETGs ($\log(M_*/M_\odot) < 11.1$) tend to be oblate-like, with their average triaxiality $T_e \sim 0.4$, while these of high-mass ETGs ($\log(M_*/M_\odot) > 11.1$) tend to be prolate-like, with their average triaxiality $T_e \sim 0.6$.
- Low-mass ETGs ($\log(M_*/M_\odot) < 11.1$) have more cold and warm orbits ($f_{\text{cold}} + f_{\text{warm}} + f_{\text{CR}} \sim 0.55$, $f_{\text{prolong}} + f_{\text{CRlong}} \sim 0.15$ and $f_{\text{box}} + f_{\text{SR}} \sim 0.3$ on average), which means they are dominated by rotation about the minor axis. High-mass ETGs ($\log(M_*/M_\odot) > 11.1$) have more long-axis tube orbits and box orbits ($f_{\text{cold}} + f_{\text{warm}} + f_{\text{CR}} \sim 0.35$, $f_{\text{prolong}} + f_{\text{CRlong}} \sim 0.25$ and $f_{\text{box}} + f_{\text{SR}} \sim 0.4$ on average). The amount of rotation about the major axis, rotation about the minor axis and centrophilic orbits are comparable for high-mass ETGs. The variation of orbital fractions as a function of stellar mass are similar to those ETGs in CALIFA sample, but not quantitatively comparable due to very different selection functions.
- There are not significant differences in the above property values between central and satellite ETGs for the same stellar masses. Thus, the variation of intrinsic orbital shapes and dark matter fractions are driven by the variation in stellar masses of galaxies. Being centrals or satellites does not have noticeable effects on these properties, at least for the inner regions covered by the MaNGA observations.
- We find that early-type galaxies more prolate-like or with higher hot orbit fractions tend to have higher close neighbour counts at $r_p \sim 40$ kpc, for similar stellar mass and colour distribution. This is consistent with the major merger origin of prolate galaxies. A galaxy has more close neighbours today may indicate a denser environment, thus have had higher major merging frequency in the past.

Having summarised our findings above, it must be remembered that all the material involving orbit circularities is at best indicative because of the observational capabilities available and the consequent deprojection degeneracies.

ACKNOWLEDGEMENTS

We thank R. C. E. van den Bosch for providing us his triaxial Schwarzschild software and M. Cappellari for making his MGE software publicly available. The modelling was accomplished on the “Zen” cluster at National Astronomical Observatories, Chinese Academy of Sciences (NAOC) and on “Venus” at Tsinghua University. This work is partly supported by the National Key Basic Research and Development Program of China (grant number 2018YFA0404501 to SM), by the National Science Foundation of China (grant numbers 11821303, 11333003, 11390372 and 11761131004 to SM). LZ acknowledges support from Shanghai Astronomical Observatory, Chinese Academy of Sciences under grant number Y895201009. GvdV acknowledges funding from the European Research Council (ERC) under the European Union’s Horizon 2020 research and innovation programme under grant agreement No 724857 (Consolidator Grant ArcheoDyn).

Funding for the Sloan Digital Sky Survey IV has been provided by the Alfred P. Sloan Foundation, the U.S. Department of Energy Office of Science, and the Participating Institutions. SDSS acknowledges support and resources from the Center for High-Performance Computing at the University of Utah. The SDSS web site is www.sdss.org.

SDSS is managed by the Astrophysical Research Consortium for the Participating Institutions of the SDSS Collaboration including the Brazilian Participation Group, the Carnegie Institution for Science, Carnegie Mellon University, the Chilean Participation Group, the French Participation Group, Harvard-Smithsonian Center for Astrophysics, Instituto de Astrofísica de Canarias, The Johns Hopkins University, Kavli Institute for the Physics and Mathematics of the Universe (IPMU) / University of Tokyo, the Korean Participation Group, Lawrence Berkeley National Laboratory, Leibniz Institut für Astrophysik Potsdam (AIP), Max-Planck-Institut für Astronomie (MPIA Heidelberg), Max-Planck-Institut für Astrophysik (MPA Garching), Max-Planck-Institut für Extraterrestrische Physik (MPE), National Astronomical Observatories of China, New Mexico State University, New York University, University of Notre Dame, Observatório Nacional / MCTI, The Ohio State University, Pennsylvania State University, Shanghai Astronomical Observatory, United Kingdom Participation Group, Universidad Nacional Autónoma de México, University of Arizona, University of Colorado Boulder, University of Oxford, University of Portsmouth, University of Utah, University of Virginia, University of Washington, University of Wisconsin, Vanderbilt University, and Yale University.

REFERENCES

- Abolfathi B., Aguado D. S., Aguilar G., et al., 2018, *ApJS*, 235, 42
- Bacon R., Copin Y., Monnet G., et al., 2001, *MNRAS*, 326, 23
- Bacon R., et al., 2017, *A&A*, 608, A1
- Berlind A. A., Frieman J., Weinberg D. H., et al., 2006, *ApJS*, 167, 1
- Bernardi M., Shankar F., Hyde J. B., Mei S., Marulli F., Sheth R. K., 2010, *MNRAS*, 404, 2087
- Binney J., Tremaine S., 2008, *Galactic Dynamics*, 2nd edn, Princeton University Press, Princeton, NJ USA
- Blanton M. R., Eisenstein D., Hogg D. W., Schlegel D. J., Brinkmann J., 2005, *ApJ*, 629, 143
- Blanton M. R., et al., 2005, *AJ*, 129, 2562
- Blanton M. R., Bershadsky M. A., Abolfathi B., et al., 2017, *AJ*, 154, 28
- Blanton M. R., Moustakas J., 2009, *ARA&A*, 47, 159
- Bluck A. F. L., et al., 2019, *MNRAS*, 485, 666

Bryant J. J., Owers M. S., Robotham A. S. G., et al., 2015, *MNRAS*, 447, 2857

Bundy K., Bershady M. A., Law D. R., et al., 2015, *ApJ*, 798, 7

Calvi R., Poggianti B. M., Fasano G., Vulcani B., 2012, *MNRAS*, 419, L14

Cappellari M., 2002, *MNRAS*, 333, 400

Cappellari M., 2016, *ARA&A*, 54, 597

Cappellari M., 2017, *MNRAS*, 466, 798

Cappellari M., Emsellem E., 2004, *PASP*, 116, 138

Cappellari M., Emsellem E., Krajnović D., et al., 2011, *MNRAS*, 413, 813

Cappellari M., McDermid R. M., Alatalo K., et al., 2013, *MNRAS*, 432, 1862

Cappellari M., Scott N., Alatalo K., et al., 2013, *MNRAS*, 432, 1709

Chabrier G., 2003, *PASP*, 115, 763

Dejonghe H., Laurent D., 1991, *MNRAS*, 252, 606

Deng X.-F., Zou S.-Y., 2009, *ApJ*, 32, 129

Dressler A., et al., 1997, *ApJ*, 490, 577

Drory N., MacDonald N., Bershady M. A., et al., 2015, *AJ*, 149, 77

Emsellem E., Monnet G., Bacon R., 1994, *A&A*, 285, 723

Emsellem E., et al., 2011, *MNRAS*, 414, 888

Fall S. M., Efstathiou G., 1980, *MNRAS*, 193, 189

Ge J., Yan R., Cappellari M., Mao S., Li H., Lu Y., 2018, *MNRAS*, 478, 2633

Genel S., Vogelsberger M., Springel V., et al., 2014, *MNRAS*, 445, 175

Goto T., et al., 2003, *MNRAS*, 346, 601

Greene J. E., Leauthaud A., Emsellem E., et al., 2018, *ApJ*, 852, 36

Gunn J. E., Siegmund W. A., Mannery E. J., et al., 2006, *AJ*, 131, 2332

Hogg D. W., et al., 2003, *ApJ*, 585, L5

Huertas-Company M., Shankar F., Mei S., Bernardi M., Aguerri J. A. L., Meert A., Vikram V., 2013, *ApJ*, 779, 29

Jin Y., Zhu L., Long R. J., Mao S., Xu D., Li H., van de Ven G., 2019, *MNRAS*, 486, 4753

Law D. R., Yan R., Bershady M. A., et al., 2015, *AJ*, 150, 19

Law D. R., Cherinka B., Yan R., et al., 2016, *AJ*, 152, 83

Li C., Kauffmann G., Heckman T. M., Jing Y. P., White S. D. M., 2008, *MNRAS*, 385, 1903

Li H., Li R., Mao S., et al., 2016, *MNRAS*, 455, 3680

Li H., et al., 2017, *ApJ*, 838, 77

Li H., Mao S., Emsellem E., et al., 2018, *MNRAS*, 473, 1489

Lintott C., Schawinski K., Bamford S., et al., 2011, *MNRAS*, 410, 166

Łokas E. L., et al., 2016, *ApJ*, 826, 227

Mathieu A., Dejonghe H., 1999, *MNRAS*, 303, 455

Minchev I., Quillen A. C., 2006, *MNRAS*, 368, 623

Moster B. P., Somerville R. S., Maulbetsch C., van den Bosch F. C., Macciò A. V., Naab T., Oser L., 2010, *ApJ*, 710, 903

Navarro J. F., Frenk C. S., White S. D. M., 1996, *ApJ*, 462, 563

Nelson D., Pillepich A., Genel S., et al., 2015, *Astronomy and Computing*, 13, 12

Park M.-J., et al., 2019, *arXiv e-prints*, arXiv:1905.02216

Pasquali A., Gallazzi A., Fontanot F., et al., 2010, *MNRAS*, 407, 937

Pasquali A., Gallazzi A., van den Bosch F. C., 2012, *MNRAS*, 425, 273

Peng Y.-jie., et al., 2010, *ApJ*, 721, 193

Planck Collaboration, Ade P. A. R., Aghanim N., et al., 2014, *A&A*, 571, A16

Postman M., Geller M. J., 1984, *ApJ*, 281, 95

Saha K., Tseng Y.-H., Taam R. E., 2010, *ApJ*, 721, 1878

Salpeter E. E., 1955, *ApJ*, 121, 161

Sánchez S. F., Kennicutt R. C., Gil de Paz A., et al., 2012, *A&A*, 538, A8

Schwarzschild M., 1979, *ApJ*, 232, 236

Smee S. A., Gunn J. E., Uomoto A., et al., 2013, *AJ*, 146, 32

Tanaka M., Goto T., Okamura S., Shimasaku K., Brinkmann J., 2004, *AJ*, 128, 2677

Tsatsi A., Lyubenova M., van de Ven G., Chang J., Aguerri J. A. L., Falcón-Barroso J., Macciò A. V., 2017, *A&A*, 606, A62

van de Ven G., de Zeeuw P. T., van den Bosch R. C. E., 2008, *MNRAS*, 385, 614

van den Bosch R. C. E., de Zeeuw P. T., 2010, *MNRAS*, 401, 1770

van den Bosch R. C. E., van de Ven G., 2009, *MNRAS*, 398, 1117

van den Bosch R. C. E., van de Ven G., Verolme E. K., Cappellari M., de Zeeuw P. T., 2008, *MNRAS*, 385, 647

Vazdekis A., et al., 2010, *MNRAS*, 404, 1639

Vogelsberger M., Genel S., Springel V., et al., 2014, *Nature*, 509, 177

Vogelsberger M., Genel S., Springel V., et al., 2014, *MNRAS*, 444, 1518

Wake D. A., Bundy K., Diamond-Stanic A. M., et al., 2017, *AJ*, 154, 86

Wang L., Wang L., Li C., Hu J., Mo H., Wang H., 2019, *MNRAS*, 484, 3865

Weinmann S. M., Kauffmann G., van den Bosch F. C., et al., 2009, *MNRAS*, 394, 1213

Weinzirl T., Jogee S., Khochfar S., Burkert A., Kormendy J., 2009, *ApJ*, 696, 411

Westfall K. B., Cappellari M., Bershady M. A., et al., 2019, *arXiv:1901.00856*

White S. D. M., 1979, *MNRAS*, 189, 831

Wuyts S., et al., 2011, *ApJ*, 742, 96

Yan R., Bundy K., Law D. R., et al., 2016, *AJ*, 152, 197

Yan R., Tremonti C., Bershady M. A., et al., 2016, *AJ*, 151, 8

Yang X., Mo H. J., van den Bosch F. C., et al., 2007, *ApJ*, 671, 153

Yang X., Mo H. J., van den Bosch F. C., 2008, *ApJ*, 676, 248

Zheng Z., Berlind A. A., Weinberg D. H., et al., 2005, *ApJ*, 633, 791

Zhu L., van den Bosch R., van de Ven G., et al., 2018, *MNRAS*, 473, 3000

Zhu L., van de Ven G., van den Bosch R., et al., 2018, *Nature Astronomy*, 2, 233

APPENDIX A: COMPARING THE ORBIT CIRCULARITY DISTRIBUTIONS WITH CALIFA RESULTS

In Fig. A1, we compare the distribution of λ_c with the results in Zhu et al. (2018b), who applied this triaxial Schwarzschild implementation to 300 CALIFA galaxies. For early-type galaxies, the CALIFA sample has more cold, warm and counter-rotating orbits, and less hot orbits than MaNGA sample on average, which means the CALIFA sample tends to have more rotating galaxies. This difference is mainly caused by the different selection functions between MaNGA and CALIFA. The MaNGA sample is missing a large fraction of fast-rotating ETGs (see Fig. A2).

APPENDIX B: COMPARISON BETWEEN SPS AND DYNAMICAL STELLAR MASS

We present a comparison of the stellar masses determined from stellar population synthesis (SPS) and our Schwarzschild modelling in Figure B1. The masses, coming from the two different modelling regimes, are clearly different. The SPS stellar masses are calculated without any knowledge of galaxy dark matter haloes, while the Schwarzschild stellar masses are determined concurrently with the dark matter masses and are affected by degeneracies between the two mass types. Fitting a straight line to the mass values gives $\log M_{*}^{\text{Schw}} = 0.88 \log M_{*}^{\text{SPS}} + 1.43$.

APPENDIX C: EXAMPLE DATA TABLE

The major properties of ten example galaxies in our sample and the corresponding modelling results are available in Table C1. The full appendix table that contains all our sample galaxies is available as supplementary material on the journal website.

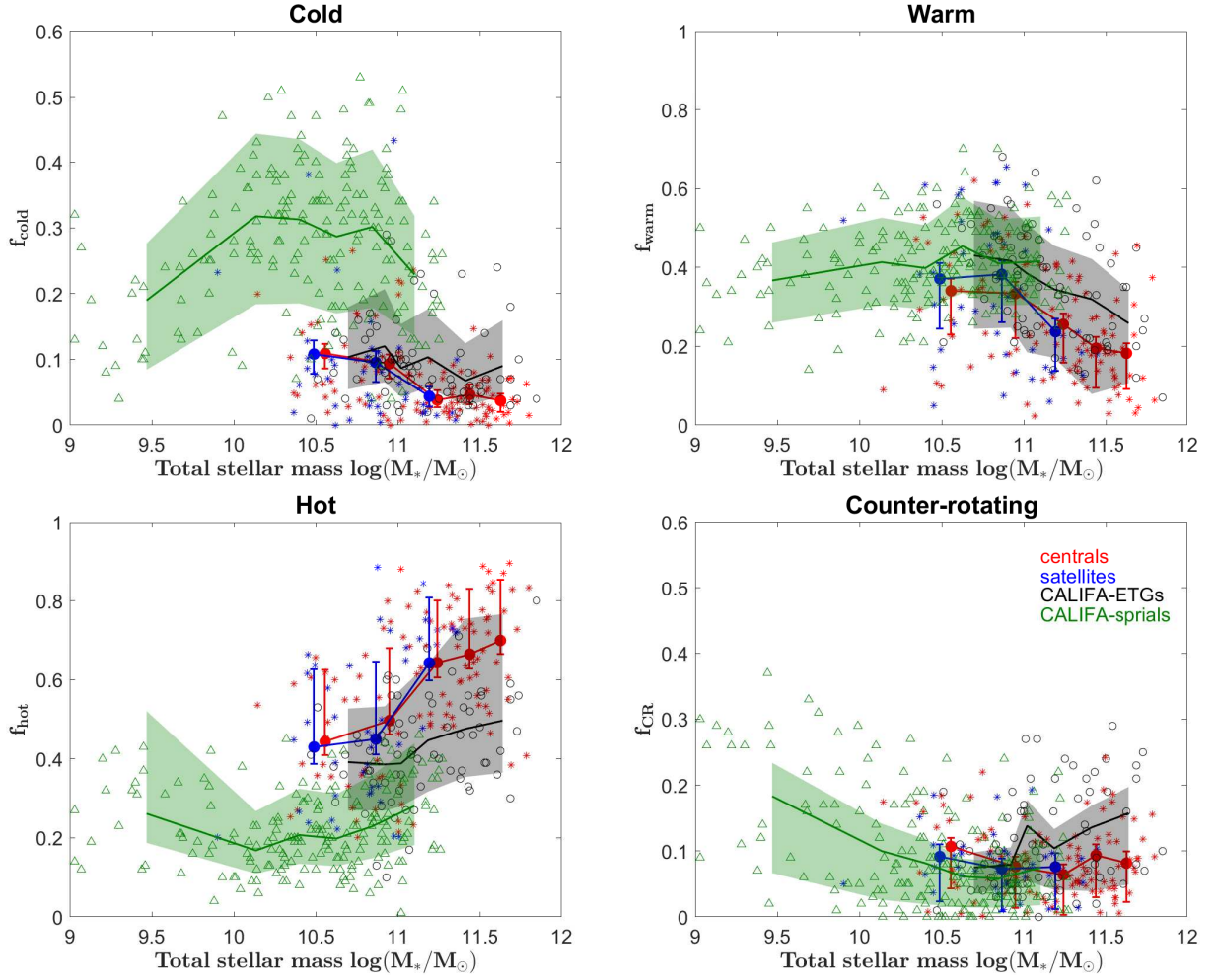


Figure A1. The luminosity fractions of cold, warm, hot and counter-rotating orbits versus total stellar mass, including results from both MaNGA and CALIFA. From top-left to bottom-right, they are: cold ($\lambda_z \geq 0.8$), warm ($0.25 < \lambda_z < 0.8$), hot ($-0.25 \leq \lambda_z \leq 0.25$) and counter-rotating ($\lambda_z < -0.25$) components. The red and blue symbols indicate our MaNGA sample and are exactly the same as Fig.12 in the manuscript. The black circles represent the results of ETGs from Zhu et al. (2018)’s CALIFA sample, while the green triangles represent that of spirals. The corresponding solid lines with shadows show the mean binned values and their uncertainties.

Table C1. The major properties of ten galaxies in our sample and the corresponding modelling results. From left to right, they are: (1) MaNGA ID; (2) the total stellar mass $\log(M_*/M_\odot)$; (3) the effective radius R_e ; (4) the dark matter fraction within one effective radius $f_{DM}(< R_e)$; (5) the medium to long axis ratio p_e , the short to long axis ratio q_e and the triaxial parameter $T_e = (1 - p_e^2)/(1 - q_e^2)$ at one effective radius; (6) the fractions of orbits f_{cold} , f_{warm} , f_{hot} and f_{CR} ; (7) the fractions of orbits $f_{prolong}$, f_{CRlong} , f_{box} and f_{SR} . Please see the journal website for the complete table.

Major properties			Schwarzschild modelling results											
MaNGA ID	$\log(M_*/M_\odot)$	R_e (kpc)	$f_{DM}(< R_e)$	p_e	q_e	T_e	f_{cold}	f_{warm}	f_{hot}	f_{CR}	$f_{prolong}$	f_{CRlong}	f_{box}	f_{SR}
1-259250	10.89	1.82	0.063	0.937	0.622	0.198	0.086	0.527	0.352	0.035	0.032	0.051	0.179	0.090
1-285095	11.50	15.94	0.754	0.980	0.697	0.077	0.045	0.182	0.535	0.242	0.001	0.023	0.309	0.201
1-285066	10.91	5.34	0.120	0.849	0.739	0.616	0.015	0.180	0.730	0.071	0.242	0.081	0.244	0.163
1-46825	11.18	7.38	0.498	0.858	0.779	0.670	0.033	0.123	0.770	0.077	0.155	0.105	0.276	0.235
1-564264	11.48	10.08	0.327	0.975	0.916	0.309	0.008	0.238	0.560	0.193	0.133	0.089	0.240	0.098
1-605419	11.69	8.58	0.001	0.997	0.946	0.057	0.072	0.456	0.384	0.089	0.050	0.047	0.075	0.211
1-585593	10.86	2.10	0.087	0.939	0.517	0.162	0.166	0.472	0.271	0.092	0.018	0.029	0.132	0.090
1-156062	11.31	12.00	0.095	0.822	0.789	0.859	0.018	0.106	0.840	0.033	0.199	0.231	0.210	0.201
1-235530	10.56	1.66	0.034	0.934	0.893	0.624	0.042	0.267	0.619	0.072	0.156	0.239	0.158	0.064
1-320584	11.68	8.92	0.440	0.913	0.754	0.387	0.071	0.305	0.550	0.074	0.109	0.079	0.292	0.071

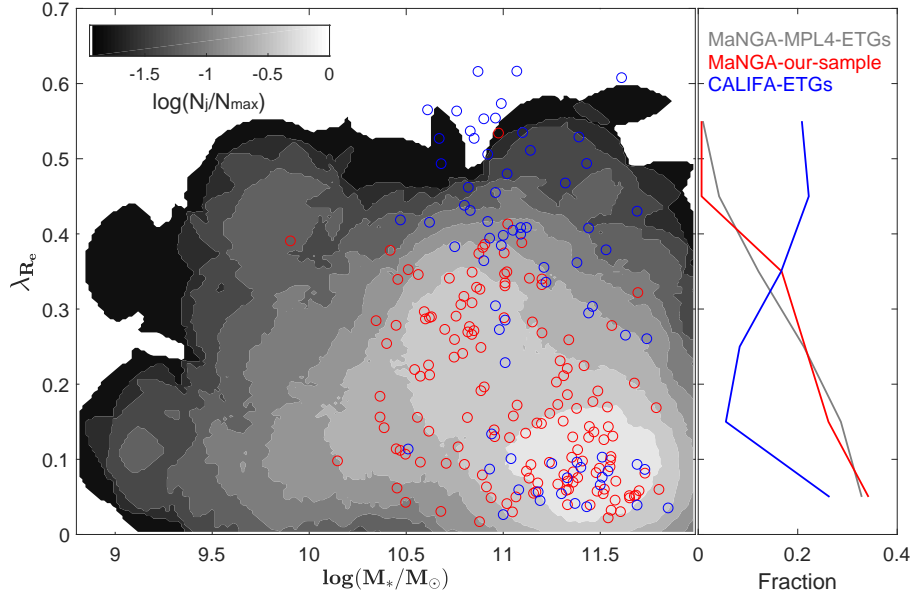


Figure A2. A widely used two-dimensional rotation indicator $\lambda_{R_e} = \frac{\langle R|V| \rangle}{\langle R\sqrt{V^2 + \sigma^2} \rangle}$ as a function of total stellar mass $\log(M_*/M_\odot)$. The red circles represent our MaNGA sample and the blue circles represent the CALIFA ETGs, while the background colour map shows the number count distribution of all ETGs in the MaNGA MPL4, with their number densities $\log(N_j/N_{\max})$ being indicated by the colour bar. N_j is the number of galaxies in mass vs λ_{R_e} bin j , and N_{\max} is the maximum of the N_j . The right panel shows the corresponding marginalised fractions of galaxies by λ_{R_e} . We can see that the distribution of λ_{R_e} is quite different between our MaNGA sample and CALIFA sample. CALIFA sample have more fast-rotating galaxies than our MaNGA sample, which is consistent with the 3D modelling results. The marginalised fractions of our sample are nearly the same as that of all the ETGs in MaNGA MPL4 (we select our sample from MaNGA MPL4), which means this difference is not caused by our sample selection criteria.

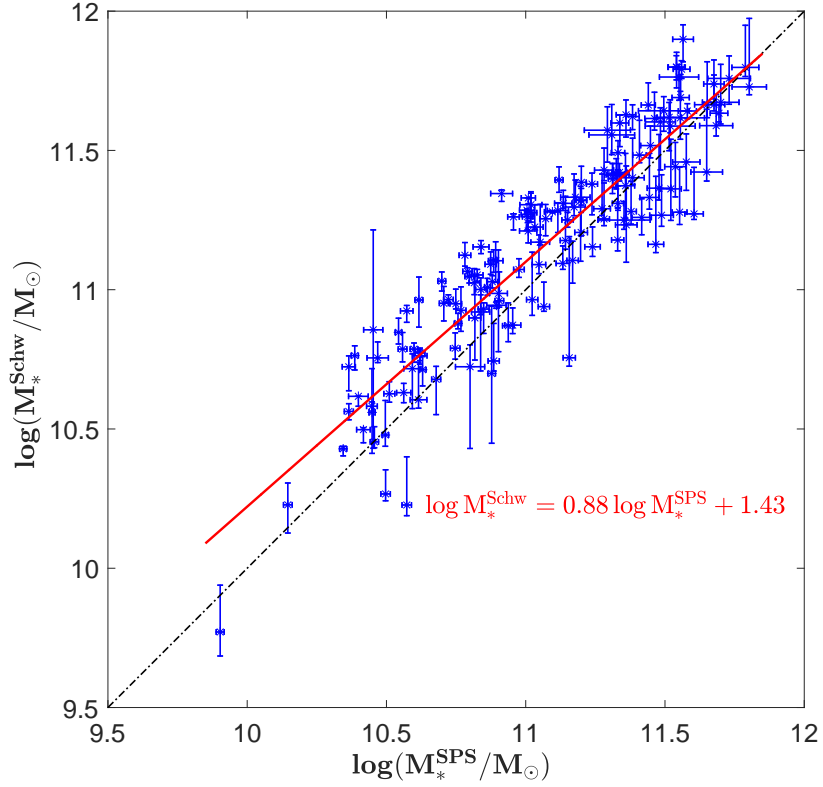


Figure B1. The comparison between stellar mass inferred from stellar population synthesis (SPS) and our Schwarzschild modelling. The horizontal axis is for SPS stellar mass while the vertical axis is for dynamical stellar mass. The best-fitting values in Schwarzschild modelling and SPS are indicated by the blue asterisks. The vertical error bars represent 1σ confidence levels in Schwarzschild modelling, while the horizontal error bars represent the scatters estimated from (Ge et al. 2018). The black dashed line indicates equal values and the red line is the linear fitted line.